Nucleic Acids Research, 2024, **52**, 9613–9629
https://doi.org/10.1093/nar/gkae637
Advance access publication date: 25 July 2024
Genome integrity, repair and replication

The translesion polymerase Pol Y1 is a constitutive component of the *B. subtilis* replication machinery

McKayla E. Marrin, Michael R. Foster, Chloe M. Santana, Yoonhee Choi, Avtar S. Jassal, Sarah J. Rancic, Carolyn R. Greenwald, Madeline N. Drucker, Denholm T. Feldman and Elizabeth S. Thrall *

Department of Chemistry and Biochemistry, Fordham University, Bronx, NY 10458, USA
*To whom correspondence should be addressed. Tel: +1 718 817 4495; Fax: +1 718 817 4432; Email: ethrall@fordham.edu

Abstract

Unrepaired DNA damage encountered by the cellular replication machinery can stall DNA replication, ultimately leading to cell death. In the DNA damage tolerance pathway translesion synthesis (TLS), replication stalling is alleviated by the recruitment of specialized polymerases to synthesize short stretches of DNA near a lesion. Although TLS promotes cell survival, most TLS polymerases are low-fidelity and must be tightly regulated to avoid harmful mutagenesis. The gram-negative bacterium *Escherichia coli* has served as the model organism for studies of the molecular mechanisms of bacterial TLS. However, it is poorly understood whether these same mechanisms apply to other bacteria. Here, we use *in vivo* single-molecule fluorescence microscopy to investigate the TLS polymerase Pol Y1 in the model gram-positive bacterium *Bacillus subtilis*. We find significant differences in the localization and dynamics of Pol Y1 in comparison to its *E. coli* homolog, Pol IV. Notably, Pol Y1 is constitutively enriched at or near sites of replication in the absence of DNA damage through interactions with the DnaN clamp; in contrast, Pol IV has been shown to be selectively enriched only upon replication stalling. These results suggest key differences in the roles and mechanisms of regulation of TLS polymerases across different bacterial species.

Graphical abstract

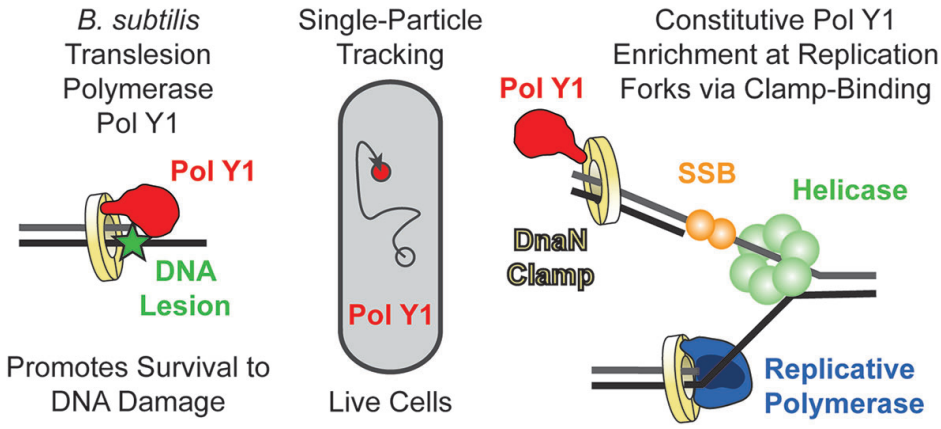

Introduction

The DNA replication machinery, the replisome, copies genomic DNA with high accuracy and efficiency (1). Yet replicative DNA polymerases can be blocked by the presence of unrepaired DNA damage on the template strand. In the DNA damage tolerance pathway translesion synthesis (TLS), conserved from bacteria to humans, specialized translesion polymerases copy damaged DNA that would otherwise stall replication (2–4). In contrast to high-fidelity replicative polymerases, most TLS polymerases are members of the error-prone Y-family (5,6). Thus, although TLS promotes cell survival under stress by avoiding the deleterious consequences of replication stalling, the activity of TLS polymerases must be tightly regulated to prevent harmful levels of mutagenesis.

The gram-negative bacterium *Escherichia coli* has served as the model system for TLS polymerase regulation in bacteria (3). *E. coli* has three TLS polymerases (Pols II, IV and V), two of which (Pols IV and V) are members of the Y-family. Pol II is a high-fidelity B-family polymerase; although capable of bypassing certain DNA lesions, its role in TLS is less clear (3,7,8). All three *E. coli* TLS polymerases are transcriptionally upregulated by the SOS DNA damage response, a pathway that induces expression of several dozen DNA damage tolerance and repair factors in response to persistent single-stranded DNA (ssDNA) (9). Pols II and IV are expressed at moderate copy

Received: October 6, 2023. **Revised:** July 3, 2024. **Editorial Decision:** July 4, 2024. **Accepted:** July 8, 2024

numbers, estimated as approximately 50 and 30 per cell, during normal growth (10,11). Upon SOS induction, they are upregulated approximately 10-fold. In contrast, Pol V is not expressed in the absence of induction and reaches levels of 15–60 copies per cell late in the SOS response (10). Pols II and IV are single gene products, whereas Pol V contains UmuC and UmuD subunits produced from the *umuDC* operon (3). Expression of Pol V is also regulated post-translationally in a pathway involving RecA that generates the active $UmuD'_2C$ form of the polymerase.

The activity of *E. coli* TLS polymerases also requires distinct protein-protein interactions. Pols IV and V must bind the ring-shaped replication processivity factor, the β clamp, to perform TLS (3); this interaction also stimulates DNA synthesis and lesion bypass by Pol II (12). In addition, all three polymerases interact with another replisome component, single-stranded DNA-binding protein (SSB), via a conserved binding site at its C-terminal tail (13,14). Recent quantitative microscopy studies have revealed that these interactions play a role in the molecular regulation of TLS polymerase activity. In particular, Pol IV is not enriched at sites of replication during normal growth (11,15), but it is selectively recruited, primarily through the interaction with SSB, in response to DNA damage or other replication perturbations (14–16). This selective enrichment likely helps to minimize mutagenesis in the absence of replication stress by limiting the access of Pol IV to the DNA template. Pol V appears to undergo a complex series of localization changes upon SOS induction; it was not observed to be enriched near sites of replication at any point after the induction of DNA damage (17). These findings suggest a model in which spatial control is an important aspect of TLS polymerase regulation in *E. coli*.

Despite advances in elucidating the molecular mechanisms of TLS in *E. coli*, there has been relatively little work in other bacterial species. Thus, it remains unclear if these mechanisms are conserved. The model low-GC gram-positive bacterium *Bacillus subtilis* represents an attractive system for exploring TLS polymerase regulation in an evolutionarily distant species. Early studies in *B. subtilis* identified two putative Y-family TLS polymerases, Pol Y1 (encoded by the *yqjH* gene) and Pol Y2 (encoded by the *yqjW gene*) (18–20). These polymerases were determined to be homologous to *E. coli* Pol IV and the UmuC subunit of Pol V, respectively (18,21). However, there are clear differences in Pol Y1 and Pol Y2 regulation and activity in comparison to their *E. coli* homologs.

Like *E. coli* Pol IV, Pol Y1 is a single gene product; uncharacteristically for a TLS polymerase, however, it is not SOS-regulated (19,22). Pol Y1 contains a conserved clamp-binding motif (CBM), a pentapeptide sequence predicted to interact with the DnaN clamp (Figure 1A) (19,23). The role of this clamp interaction in damage tolerance has not been determined, but a reduction in Pol Y1-mediated untargeted mutagenesis was observed upon mutation of the Pol Y1 CBM (19) and a Pol Y1-DnaN interaction was detected in a yeast two-hybrid assay (24). The importance of other protein-protein interactions for Pol Y1 activity is unknown, although the same yeast two-hybrid assay detected an interaction with Pol I (24) and bioinformatics analysis suggested a possible interaction with RecA through a domain similar to the RecA N-terminal domain (RecA-NT) (Figure 1A) (25). Pol Y1 promotes survival upon treatment with various DNA damaging agents, including 4-nitroquinoline 1-oxide (4-NQO) and UV radiation (18,26). In contrast, Pol IV does not promote survival or mutagenesis upon UV exposure; instead, Pol V bypasses UV lesions in *E. coli* (27). Finally, Pol Y1 has been implicated in responding to replication-transcription conflicts and appears to act in the transcription-coupled nucleotide excision repair (NER) pathway (26). Similarly, there is evidence that Pol IV may play a role in transcription-coupled NER or TLS pathways in *E. coli* (28,29).

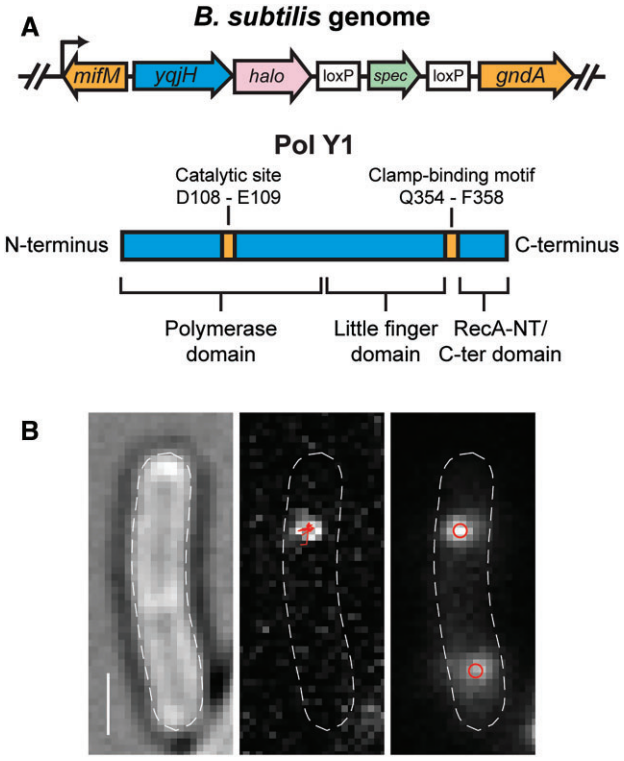

Figure 1. (**A**) Cartoons of (top) Pol Y1-Halo (*yqjH-halo*) fusion and context in *B. subtilis* genome and (bottom) Pol Y1 domain organization and key residues. (**B**) Representative micrographs recorded with 13.9 ms integration time. Left: transmitted white light micrograph of *B. subtilis* cell with overlaid cell outline and 1 μm scale bar. Middle: fluorescence micrograph of single Pol Y1-Halo-JFX_{554} molecule with overlaid trajectory. Right: fluorescence micrograph of DnaX-mYPet foci with overlaid centroids.

In this study, we use *in vivo* single-molecule fluorescence microscopy to quantify the location and dynamics of Pol Y1, both during normal growth and upon DNA damage with the drug 4-NQO. We observe static and mobile populations of Pol Y1 under both conditions, representing Pol Y1 molecules bound to DNA or diffusing in the cytoplasm, respectively. Notably, we find that the static population of Pol Y1 is moderately enriched near sites of replication during normal growth, in contrast to *E. coli* Pol IV. This enrichment does not require Pol Y1 catalytic activity, but it does require interactions with the DnaN clamp. Surprisingly, although Pol Y1 promotes survival in response to treatment with 4-NQO, there is little change in Pol Y1 localization and dynamics upon 4-NQO treatment, again in contrast to previous observations for Pol IV. Further, Pol Y1 does not contribute to mutagenesis upon 4-NQO treatment. Our results reveal significant differences in the activity of TLS polymerases across different bacterial species.

Materials and methods

Bacterial strain construction

All bacterial strains were based on the wild-type (WT) *B. subtilis* background PY79 (30,31). New bacterial strains were constructed by transformation of double-stranded DNA (dsDNA) fragments generated by polymerase chain reaction (PCR) and Gibson assembly (32) or of genomic DNA. Transformants were selected on antibiotic plates and validated by diagnostic PCR and Sanger DNA sequencing of the modified locus. All oligonucleotides and bacterial strains used in this study are listed in Supplementary Tables S1 and S2. Detailed strain construction information is provided in the Supplementary Methods.

Survival assays

Glycerol stocks were streaked onto LB Lennox agar plates containing the appropriate antibiotics for strain selection (spectinomycin at 100 μg/ml or chloramphenicol at 5 μg/ml) and incubated overnight at 37°C. Liquid cultures were prepared in LB Lennox media. The day before the experiment, a 2.5 ml culture of each strain was inoculated with a single colony and a second 2.5 ml culture was inoculated with a 1:100 dilution of the first culture. Both cultures were grown overnight for approximately 16 h at 22°C shaking at 225 rpm. The following morning, fresh cultures of 3 ml volume with an optical density at 600 nm (OD_{600nm}) of 0.05 were prepared using the overnight culture with $OD_{600nm} = 0.4–1.0$. The fresh cultures were then grown at 37°C shaking at 225 rpm for approximately 3.5 h. LB Lennox agar plates were poured the day of the experiment and supplemented with a 1:1000 dilution of a freshly prepared solution of 4-NQO in dimethylformamide (DMF), giving final concentrations of 0, 0.05, 0.075 or 0.1 μM 4-NQO. Serial 10-fold dilutions of the fresh cultures were prepared in LB Lennox media and 200 μl aliquots of appropriate dilutions were spread on the 4-NQO plates using glass beads. The plates were incubated at 37°C overnight, colonies were enumerated the following morning, and survival rates were determined for each drug concentration relative to the no drug plate. At least three independent replicates were performed for each experiment.

Rifampicin resistance mutagenesis assays

Rifampicin (Rif) resistance mutagenesis assays were performed following a procedure adapted from the literature (19,33). As described in the previous section, cultures were inoculated and grown for approximately 3.5 h in LB Lennox media. Cultures were then split into two aliquots, one of which was treated with 10 μM 4-NQO by addition of a 1:1000 dilution of a freshly prepared 10 mM 4-NQO solution in DMF. Both treated and untreated cultures were grown for an additional 1 h under the same conditions. Cells were then pelleted by 5 min of centrifugation in a Fisher Scientific Centrific Centrifuge on power level 8.5, resuspended in 1 ml of fresh LB Lennox media, then pelleted again by centrifugation at 3500 × *g* for 2.5 min. Cell pellets were resuspended in 1 ml of fresh media, centrifuged again, and resuspended in 10 ml of fresh LB Lennox media. The cultures were grown overnight as before. The following morning, LB Lennox agar plates were prepared either with or without supplementation with a 1:1000 dilution of a freshly prepared solution of 10 mg/ml Rif in dimethylsulfoxide (DMSO), giving a final Rif concentration of 10 μg/ml. After approximately 22–24 h of growth, overnight cultures were concentrated to $OD_{600nm} \approx 20$ by centrifugation in a Fisher Scientific Centrific Centrifuge as described before. Concentrated cultures were spread on Rif^+ plates, then serially diluted to $OD_{600nm} \approx 10^{-5}$ and spread on Rif^- plates. The plates were incubated overnight at 37°C, colonies were enumerated the following morning, and mutagenesis rates were determined by comparing the number of Rif^R colony-forming units (CFUs) per ml to the total number of CFUs/ml. Six independent experimental replicates were performed.

Cell culture and sample preparation for microscopy

Glycerol stocks were streaked onto LB Lennox agar plates as described previously. Liquid cultures were grown in freshly prepared $S7_{50}$-sorbitol minimal medium (34), in which glutamate was used at 20 mM concentration and sorbitol at 0.4% concentration. The day before the experiment, a single colony was picked and used to inoculate a culture in 2.75 ml media, which was then added at 1:10 dilution into 2.25 ml media, yielding two cultures of 2.5 ml volume. Both cultures were grown overnight for approximately 16 h at 30°C shaking at 225 rpm. The following morning, the culture with $OD_{600nm} = 0.4–1.0$ was used to inoculate a 25 ml culture for imaging to an initial $OD_{600nm} = 0.005–0.02$. Imaging cultures were grown at 37°C shaking at 225 rpm until reaching early exponential phase, or $OD_{600nm} \approx 0.1–0.2$.

When a culture was ready to harvest for microscopy, a 3 ml aliquot was pelleted by centrifugation at 3500 × *g* for 2.5 min. All but 200 μl of the supernatant was aspirated and the cell pellet was resuspended to a final volume of 500 μl with fresh media. The sample was labeled by adding a 1:1000 dilution of Janelia Fluor X 554 (JFX_{554}) (35) HaloTag (36) ligand dissolved in DMSO. The sample was then incubated for 15 min at 37°C shaking at 225 rpm. The cell suspension was pelleted by centrifugation as before and the supernatant was removed. The cells were washed by adding 1 ml of fresh media, resuspending the pellet, and centrifuging again. Most of the supernatant was removed and the pellet was resuspended in the remaining few μl of liquid. A small volume (<1 μl) of the concentrated cell suspension was deposited on an agarose pad and sandwiched between two coverslips for imaging.

For control experiments to test the effect of JFX_{554} labeling on cell morphology and the DnaX foci, unlabeled samples were prepared for microscopy following a simplified version of the procedure above. A 1.5 ml aliquot was pelleted by centrifugation at 3500 × *g* for 2.5 min, most of the supernatant was aspirated, and the cell pellet was resuspended in the remaining few μl of liquid. The concentrated cell suspension was used to prepare an imaging sample as described previously.

Agarose pads were prepared by melting GTG agarose (NuSieve) at 3% concentration in $S7_{50}$-sorbitol media at 65°C for 15–30 min. Coverslips were cleaned by rinsing with ethanol and deionized (DI) H_2O and dried in a nitrogen gas stream. To cast an agarose pad, 500 μl of molten agarose was deposited between two coverslips and left to cool for 20–30 min until solid. Coverslips in contact with the microscope objective were cleaned by 30 min cycles of sonication alternating between alcohol and 1 M KOH twice each, stored in DI H_2O and rinsed with DI H_2O before use.

Sample treatment for microscopy

For 4-NQO treatment of imaging cultures, a freshly prepared 4-NQO solution in DMF was diluted 1:1000 into an early exponential phase ($OD_{600nm} \approx 0.1–0.2$) culture. The treated culture was grown shaking at 37°C and 225 rpm for an additional 1 or 2 h. The effect of the treatment on cell growth was determined by measuring the number of CFUs/ml in each culture before and after treatment. In brief, an aliquot of culture was diluted serially in 0.9% NaCl and a 200 µl volume was deposited on plain LB Lennox agar plates and spread with glass beads. Plates were incubated overnight at 37°C, colonies were enumerated, and the number of CFUs/ml was calculated.

To determine whether the JFX_{554} HaloTag labeling process affected cell growth, we followed a similar approach. Two 3 ml aliquots were harvested from an early exponential phase ($OD_{600nm} \approx 0.1–0.2$) culture and one aliquot was labeled with 2.5 nM JFX_{554} HaloTag ligand. Cultures were grown for an additional 1 h and then serially diluted, plated, and incubated overnight as described in the previous paragraph. Colonies were enumerated and the fold-change in CFUs/ml was compared for labeled and unlabeled cultures.

For fixed cell imaging experiments, a protocol was adapted from the literature (15,37). In brief, a 4.5 ml aliquot of culture was harvested in early exponential phase ($OD_{600nm} \approx 0.1–0.2$) and concentrated by two rounds of centrifugation at 3500 × *g* for 2.5 min. The resulting cell pellet was resuspended at 3× concentration in a 2.5% solution of formaldehyde in phosphate buffered saline (PBS) and incubated with gentle shaking at room temperature for 45 min. Cells were then pelleted by centrifugation as before and resuspended in 500 µl of fresh $S7_{50}$-sorbitol media, then labeled with JFX_{554} HaloTag ligand at a lower concentration of 250 pM and prepared for microscopy as described in the previous section. An alternative fixation protocol based on prior reports (26,38), which used a higher 4% formaldehyde concentration and a longer 1 h incubation time, gave similar results.

Microscopy

Fluorescence imaging was performed on a Nikon Ti2-E microscope equipped with a Nikon CFI Apo 100×/1.49 NA total internal reflection fluorescence (TIRF) objective lens and a Hamamatsu ImageEM C9100-23BKIT EMCCD camera. An additional internal magnification of 1.5× resulted in a pixel size of approximately 106 nm, determined by measuring a calibration grid (Thorlabs R1L3S2P). Fluorescence excitation was provided by 514 nm (150 mW) and 561 nm (200 mW) Coherent Sapphire lasers; laser powers were adjusted using neutral density filters. The individual laser beams were first expanded with a telescope and then passed through excitation filters (Chroma ZET514/10x and ZET561/10×) before being combined with a mirror and dichroic filter (Chroma ZT514rdc-UF2). After passing through a second dichroic filter (Chroma ZT405rdc-UF2) for an unused laser line, the beams were then expanded with a second telescope and focused to the objective back focal plane (BFP) using a 400 mm focal length lens (Thorlabs AC508-400-A) mounted on a micrometer stage. Highly inclined thin illumination (39), or near-TIRF, excitation was achieved by translating the lens to move the focused beam away from the center of the objective BFP. The microscope contained a TIRF filter cube (Chroma) with multi-band dichroic and emission filters (Chroma ZT405/514/561rpc-UF2 and ZET442/514/561m) and a longpass filter (Chroma ET525lp) to remove the unnecessary short-wavelength passband. Brightfield images of cells were recorded with white light transillumination. The microscope was equipped with a computer-controlled translation stage (Mad City Labs MicroStage). Computer-controlled shutters (Vincent Uniblitz VS14ST0 and VMM-D4 driver) were used to automate laser excitation.

Movies were recorded with either a short integration time (13.9 ms) to enable tracking of all labeled molecules or a long integration time (250 ms) for selective imaging of static molecules (15,37). For single Pol Y1-Halo-JFX_{554} molecules, 561 nm laser powers of approximately 15 and 5 W/cm^2 were used for short- and long-exposure imaging, respectively. For DnaX-mYPet foci, 514 nm laser powers of approximately 1 and 0.1 W/cm^2 were used for short- and long-exposure imaging, respectively. HBsu-mYPet short-exposure imaging used a 514 nm laser power of approximately 0.5 W/cm^2. Most movies commenced with 100 frames of 514 nm excitation before 561 nm excitation. For HBsu-mYPet imaging, 500 frames of 514 nm excitation were recorded first in order to bleach the strong mYPet signal.

To check for any apparent offset between the 514 and 561 nm channels due to chromatic aberrations in the microscope optics, we imaged 0.1 µm diameter TetraSpeck beads (Thermo Fisher Scientific #T7279), used u-track to determine the bead centroids, and compared the apparent centroid positions under 514 and 561 nm excitation. We found an offset of approximately 11 nm between the two channels, indicating that chromatic effects are negligible. The localization precision was determined by imaging Pol Y1-Halo-JFX_{554} in fixed cells. As described previously, the mean *x* and *y* positions were determined for each trajectory and then the *x* and *y* offsets for each localization were determined relative to the mean positions. The *x* and *y* offset values were aggregated across all trajectories and the resulting distributions were fit to Gaussian functions. The localization precisions in *x* and *y* were given by the Gaussian widths σ_x and σ_y. The lateral localization precision σ_{xy} was determined as:

$$\sigma_{xy} = \left(\sigma_x^2 + \sigma_y^2\right)^{1/2}$$

For short-exposure imaging, $\sigma_x = 26.5$ nm, $\sigma_y = 26.0$ nm and $\sigma_{xy} = 37.1$ nm. For long-exposure imaging, $\sigma_x = 17.4$ nm, $\sigma_y = 18.1$ nm and $\sigma_{xy} = 25.1$ nm.

Image analysis

Automated image analysis was performed using the MATLAB-based packages MicrobeTracker (v. 0.937) (40) and u-track (v. 2.1.1) (41,42), in addition to custom MATLAB code. As the initial step, cell segmentation was performed on brightfield images using MicrobeTracker to generate cell outlines. Spot detection was performed within each individual cell outline using the u-track point source detection algorithm, which fits spots to symmetrical two-dimensional (2D) Gaussian approximations of the point spread function (PSF); fit parameters consisted of the *x* and *y* centroid positions, the Gaussian width, the Gaussian amplitude, and the background offset. Detected spots were then linked in trajectories using the u-track tracking algorithm, which dynamically sets a search radius for frame-to-frame linking of particles within specified lower and upper distance bounds. Nearest neighbor distance was not used to expand the search radius. Analysis settings for specific movie types are described below;

if not otherwise noted, default spot detection and tracking parameters were used. A small number of cells were manually excluded from analysis if they contained an unusually high fluorescence background.

For short-exposure Pol Y1-Halo imaging, the u-track significance threshold $\alpha = 10^{-5}$ was used; this parameter determines the stringency of spot detection, with smaller values of α requiring a higher signal-to-noise ratio for detection. Gaps of one frame duration were allowed in trajectories to account for missed localizations due to fluorophore blinking or failed detection. Tracks were required to contain at least two localizations, although tracks containing fewer than five localizations were excluded from subsequent analysis with the exception of Spot-On diffusion analysis. The Brownian search radius multiplier factor was set to 5; this parameter adjusts the search radius for each particle based on its previous motion.

For long-exposure Pol Y1-Halo imaging, a u-track significance threshold of $\alpha = 10^{-6}$ was used and no gaps were allowed in trajectories. The upper bound on the Brownian search radius was set to 3 pixels. After spot detection and tracking, static molecules were identified by requiring the average of the PSF width for all localizations within a trajectory to be in the range of 0.703–2.145 pixels (74.5–227.4 nm). These values were taken as the mean value ± two standard deviations of a Gaussian fit to the distribution of PSF widths observed in fixed cells (Supplementary Figure S1C); this requirement minimizes spurious detection of mobile molecules, which give rise to spots with broader PSFs in long-exposure imaging (15,37). We note that in addition to the primary peak in the PSF width distribution, there is a small shoulder at larger widths, which likely reflects a small population of mobile molecules remaining in the cell after fixation. Although we tested two different protocols (see *Sample Treatment for Microscopy*), we were unable to eliminate this small mobile population. However, the analysis results are not highly sensitive to the exact PSF width threshold used to identify static mobiles.

For both exposure times, DnaX-mYPet foci were analyzed by generating an average projection of the first 20 frames of 514 nm excitation. Spot detection was performed on the resulting average image as described above, using a u-track significance threshold of $\alpha = 10^{-5}$. To remove a small number of false positive spots, the Gaussian background value was required to be above the camera offset level of 2065 counts.

Imaging dataset

In general, experiments were performed on at least two different days with at least three independent replicates, defined as separate imaging cultures. Some control experiments, however, were performed with only two replicates. In all cases, individual replicates were checked for consistency. Supplementary Table S3 lists the number of imaging days, replicates, cells and tracks or foci for all imaging data.

Data analysis

Diffusion coefficient analysis (MSD approach)

Apparent 2D diffusion coefficients (D^*) were calculated from the mean squared displacement (MSD) of short-exposure trajectories with at least five localizations as:

$$D^* = \frac{MSD}{4\Delta t}$$

where Δt is the time interval between subsequent localizations. The MSD is given by:

$$MSD = \frac{1}{N-1}\sum_{i=1}^{N-1}(x_{i+1}-x_i)^2 + (y_{i+1}-y_i)^2$$

where x_i and y_i are the track coordinates in the ith frame.

The resulting distributions for D^* revealed the presence of more than one diffusing species. These probability distributions were fit to a model for three diffusing species, which gave the best agreement with the experimental results. For trajectories containing exactly four steps, the following analytical expression describes the probability distribution:

$$f(x; D_1, D_2, D_3, A_1, A_2, A_3) = A_1\frac{(4/D_1)^4}{6}x^3e^{-4x/D_1} + A_2\frac{(4/D_2)^4}{6}x^3e^{-4x/D_2} + A_3\frac{(4/D_3)^4}{6}x^3e^{-4x/D_3}$$

where A_n is the fraction of molecules in the nth species and D_n represents the diffusion coefficient of that species (16,43). Fitting was performed subject to the normalization constraint:

$$A_1 + A_2 + A_3 = 1$$

Longer trajectories were truncated to retain only the first four steps before use in this analysis.

To differentiate between static and mobile Pol Y1 molecules using a single D^* threshold value, we generated a distribution of observed D^* values in fixed cells (Supplementary Figure S1B). Molecules were considered static if they had a D^* value less than the mean of a Gaussian fit to this distribution plus two standard deviations, corresponding to a cutoff of $D^* < 0.14$ μm^2/s. In addition to the main peak, we note that there is a small tail at larger values of D^*. Like the shoulder in the distribution of PSF widths in fixed cells (Supplementary Figure S1C), we attribute this tail to the small population of mobile molecules remaining in the cell. As for the PSF width threshold, the analysis results are not highly sensitive to the exact D^* threshold value used to identify static molecules.

Diffusion coefficient analysis (Spot-On)

As an alternative approach to quantify Pol Y1 mobility, we implemented the Spot-On algorithm, which analyzes particle diffusion using a kinetic modeling framework (44). Pol Y1 trajectories of any length were fit to a two-state model with one static and one mobile population; although jump length distributions were not fit perfectly by this two-state model, we followed recommendations of Hansen, et al. to use a two-state model unless there was a clear reason to expect two mobile populations. Analysis was performed with the following parameters: TimeGap = 14.7 ms, dZ = 0.7 μm, GapsAllowed = 1, BinWidth = 0.01 μm, Timepoints = 4, JumpsToConsider = 4, MaxJump = 5.05 μm, ModelFit = 2 (use CDF fitting), DoSingleCellFit = 0, NumberOfStates = 2, FitIterations = 3, LocError = 0.037 μm (our measured lateral localization precision), UseWeights = 0, D_Free = [0.5 25] (in μm^2/s), D_bound = [0.0001 0.1] (in μm^2/s).

Cellular localization analysis

To allow comparison of Pol Y1-Halo and DnaX-mYPet localization across cells of different sizes and orientations, cell coordinates were rotated and normalized so that x and y coordinates spanned values from 0 to 1 along the long and short cellular axes, respectively (15). First, one cell pole was set to a coordinate of (0,0) by subtracting the appropriate offset values from the cell outline x and y coordinates. The cell outline was then rotated by the angle between the two cell poles and the x-axis to align the cellular long axis with the x-axis. The cell outline x and y coordinates were divided by the cell length and width respectively and offset again such that the coordinates ranged from 0 to 1 along both cellular axes. The same transformations were then applied to the coordinates of Pol Y1 trajectories or DnaX foci to convert them to normalized coordinates. Finally, distributions of normalized x and y coordinates were generated. For Pol Y1, the mean x and y positions for each trajectory were compiled.

Nucleoid profile analysis

The cellular localization and morphology of the nucleoid was determined by calculating average HBsu-mYPet intensity profiles, following an approach described previously (15). An average projection of the first 50 frames of HBsu-mYPet imaging was generated for analysis. For each cell, the fluorescence intensity along the centerline of the cellular long axis was determined by rounding the centerline coordinate to the nearest pixel and taking the intensity of each centerline pixel. The x coordinates of the resulting intensity profile were divided by the cell length to convert them to normalized coordinates ranging from 0 to 1. The resulting intensity profiles were interpolated to get intensity values at a standard set of x coordinates. After interpolation, the single-cell profiles were averaged to give a mean nucleoid intensity profile, which was then min-max normalized to give relative intensity values ranging from 0 to 1.

Radial distribution function analysis

Intracell colocalization between individual Pol Y1-Halo molecules and DnaX-mYPet foci was quantified using radial distribution function analysis (15,45,46). First, the average distance between each Pol Y1 trajectory and the closest DnaX focus was determined. Next, the same number of Pol Y1 localizations were randomly simulated within the same cell outline and the corresponding Pol Y1-DnaX distances were determined. Distributions of experimental and random Pol Y1-DnaX distances were generated by repeating this analysis for all cells in the dataset. If Pol Y1 were randomly localized relative to DnaX, these distance distributions would be identical. Finally, the radial distribution function, $g(r)$, was generated by normalizing the experimental distribution by the random distribution. Random localization is indicated by $g(r) \approx 1$ across all Pol Y1-DnaX distances r, whereas enrichment of Pol Y1 near DnaX is indicated by $g(r) > 1$ at short distances. To minimize variability, this procedure was repeated 100 times using 100 different random distance distributions and the resulting 100 $g(r)$ curves were averaged. The standard error of the mean (S.E.M.) for these 100 $g(r)$ curves are reported in Supplementary Table S4. As a confirmation that the sample size was adequate, an independent random Pol Y1-DnaX distance distribution was generated and 100 random $g(r)$ curves were calculated and averaged in the same manner. Deviations in the resulting random $g(r)$ curve from 1 are due to the finite sample size. This radial distribution function approach accounts for spurious Pol Y1-DnaX colocalization due to cellular confinement; it also corrects for differences in cell size or number of DnaX foci across different treatment conditions.

Binding lifetime analysis

The Pol Y1 binding lifetime was measured by selectively imaging static molecules using long 250 ms integration times. For each static trajectory, the apparent binding lifetime was taken as the trajectory duration. Because this apparent binding lifetime includes both true dissociation events and events where the JFX_{554} fluorophore photobleached, observed apparent binding lifetimes (τ_{app}) were corrected by the photobleaching lifetime of JFX_{554} (τ_{bleach}) to give a photobleaching corrected binding lifetime (τ_{bound}) (37):

$$\tau_{bound} = \frac{\tau_{app}\tau_{bleach}}{\tau_{bleach} - \tau_{app}}$$

To determine τ_{bleach}, JFX_{554}-labeled Pol Y1 was imaged in fixed cells, where dissociation does not occur. The lifetimes τ_{app} and τ_{bleach} were determined from single exponential fits to the distributions of measured trajectory durations. Because these durations are not well fit by a single exponential and include both short and long timescale decays, tracks less than five frames in duration were excluded from the fits to capture the long timescale behavior.

Statistical analysis

Distributions were compared using a two-sided Wilcoxon rank sum test, with a threshold of $P < 0.05$ for statistical significance.

Results

Creation and validation of a functional Pol Y1 fusion

To visualize single copies of Pol Y1 in live *B. subtilis* cells, we created a C-terminal fusion of the self-labeling HaloTag (36) to the endogenous copy of the *yqjH* gene (Figure 1A). By treating cells with a low (2.5 nM) concentration of a Janelia Fluor X 554 (JFX_{554}) HaloTag ligand (35), we were able to sparsely label Pol Y1 in live cells (Figure 1B, left panel) with the bright and photostable fluorophore JFX_{554}, enabling detection and tracking of single Pol Y1 molecules (Figure 1B, middle panel). In addition, we introduced an orthogonal fusion of the yellow fluorescent protein mYPet (47) to the clamp-loader component DnaX; this DnaX-mYPet fusion forms bright and distinct foci, allowing simultaneous visualization of sites of DNA replication in the cell (Figure 1B, right panel) (48–51). We note that a single DnaX focus could represent either one replication fork or two replication forks localized within the resolution limit of the microscope; a previous imaging study determined that sister replication forks remain colocalized, with sub-diffraction limit separation, over the course of the cell cycle in *B. subtilis* (50). To visualize the entire population of Pol Y1 molecules, we imaged cells with a short 13.9 ms exposure time. Alternatively, to resolve immobile Pol Y1 molecules selectively, we used a longer 250 ms exposure time; long exposure times blur out the fluorescence signal from rapidly-moving molecules such that only immobile molecules are detected (15,37).

High levels of background fluorescence have been observed in *B. subtilis* cells, potentially leading to detection of false posi-

tives in sensitive single-molecule fluorescence microscopy (52). To address this possibility, we imaged a strain bearing only the DnaX-mYPet fusion labeled with the same 2.5 nM JFX_{554} dye concentration and analyzed the resulting false positive signal. Results are shown in the Supporting Information for localization (Supplementary Figures S2A and B) and diffusion (Supplementary Figures S6A–D) measurements. In all cases, we observed almost no false positive signal in comparison to the true Pol Y1-Halo-JFX_{554} signal.

We assessed the functionality of the Pol Y1-Halo fusion by assaying cell sensitivity to the DNA damaging agent 4-NQO, which generates DNA lesions on guanine and adenine bases, including quinoline adducts to the guanine N^2 position (53–55). Consistent with a previous report (26), we find that cells lacking Pol Y1, but not Pol Y2, are sensitized to 4-NQO treatment (Figure 2A). Cells bearing the Pol Y1-Halo fusion are indistinguishable from WT, as are cells containing both the Pol Y1-Halo and DnaX-mYPet fusions (Figure 2B). We also constructed C-terminal Pol Y1 fusions to mYPet and to the photoactivatable fluorescent protein Dendra2 (56,57), the latter of which was slightly sensitized to 4-NQO treatment relative to WT (Supplementary Figure S1A).

To determine whether the JFX_{554} labeling procedure was harmful to the cells, we first assessed its effect on culture growth. Identical aliquots of imaging cultures were removed and either not labeled or labeled with 2.5 nM JFX_{554}, then grown for 1 h; although the normal labeling time for microscopy was 15 min, we chose a longer 1 h incubation for better detection of any growth defects. We quantified the fold-change in the number of CFUs/ml before and after labeling or mock labeling by plating cells and counting colonies. The number of CFUs/ml increased by a factor of 2.3 ± 0.3 (mean ± std.) for unlabeled and 2.0 ± 0.2 (mean ± std.) for labeled cultures, indicating little or no effect of the labeling on cell growth. Additionally, we tested for any effects of labeling on cell morphology by imaging unlabeled cells and quantifying the cell size. The mean cell length was marginally larger than the mean value in labeled cells (mean ± S.E.M.: 3.63 ± 0.03 μm versus 3.48 ± 0.03 μm), and the mean cell width was marginally smaller (mean ± S.E.M.: 0.670 ± 0.004 μm versus 0.695 ± 0.002 μm). Although both differences were statistically significant ($P < 0.05$), they were < 5% in magnitude. Further, the mean areas in unlabeled versus labeled cells were not significantly different (mean ± S.E.M.: 2.45 ± 0.05 μm^2 versus 2.43 ± 0.03 μm^2; $P > 0.05$). Taken together, these results suggest that the JFX_{554} labeling procedure is minimally perturbative to the cells.

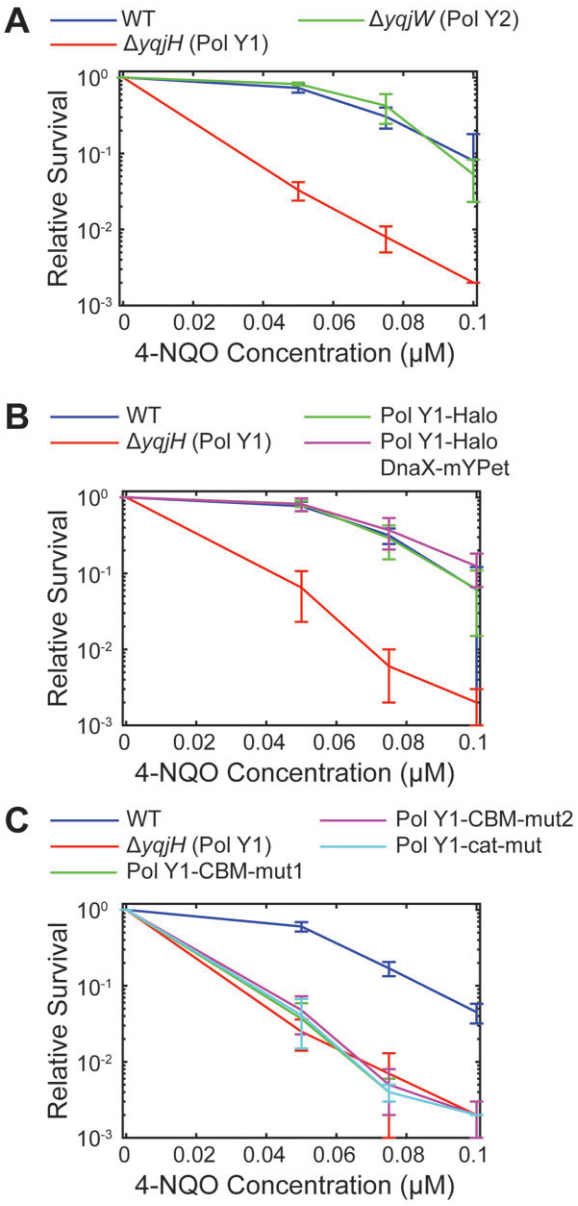

Figure 2. Relative survival of *B. subtilis* strains treated with different concentrations of 4-NQO. (**A**) WT Pol Y1, Pol Y1 knockout, and Pol Y2 knockout strains. (**B**) WT Pol Y1, Pol Y1 knockout, Pol Y1-Halo fusion, and Pol Y1-Halo fusion plus DnaX-mYPet fusion strains. (**C**) WT Pol Y1, Pol Y1 knockout, Pol Y1 clamp-binding mutant (Pol Y1-CBM-mut1 and Pol Y1-CBM-mut2), and Pol Y1 catalytically inactive mutant (Pol Y1-cat-mut) strains. Error bars show standard deviation of at least three replicates.

Pol Y1 is moderately enriched near sites of replication during normal growth

In *E. coli*, TLS polymerases are largely excluded from the replication fork in the absence of DNA damage or other replication perturbations (11,15,16). First, we asked whether the same was true for Pol Y1 by comparing the average cellular localization of Pol Y1 and DnaX. We found that DnaX foci were primarily localized at the quarter and three-quarter positions along the long cell axis and at midcell along the short cell axis (Figure 3A and B). Although each individual DnaX focus is tightly localized (Figure 1B, right panel), the exact position of the DnaX foci in each individual cell is variable; as a result, the average localization distribution is broader. This localization is consistent with previous reports of replication fork positioning in *B. subtilis* (49,50). Cells typically contained between one and two DnaX foci (mean ± S.E.M.: 1.67 ± 0.03). Average DnaX localization (compare Supplementary Figure S2D to S3C) and number of foci (mean ± S.E.M.: 1.65 ± 0.05; $P > 0.5$ relative to labeled) were almost identical in unlabeled cells, further confirming the minimal effect of JFX_{554} labeling.

Pol Y1 localization was like that of DnaX, with strong enrichment at the quarter and three-quarter cell long axis positions and at midcell along the short axis (Figure 3C). We observed similar localization using a longer 250 ms integration time to resolve static Pol Y1 molecules selectively, but with greater Pol Y1 localization at the midcell position along the long cell axis (Supplementary Figures S3A and C). To con-

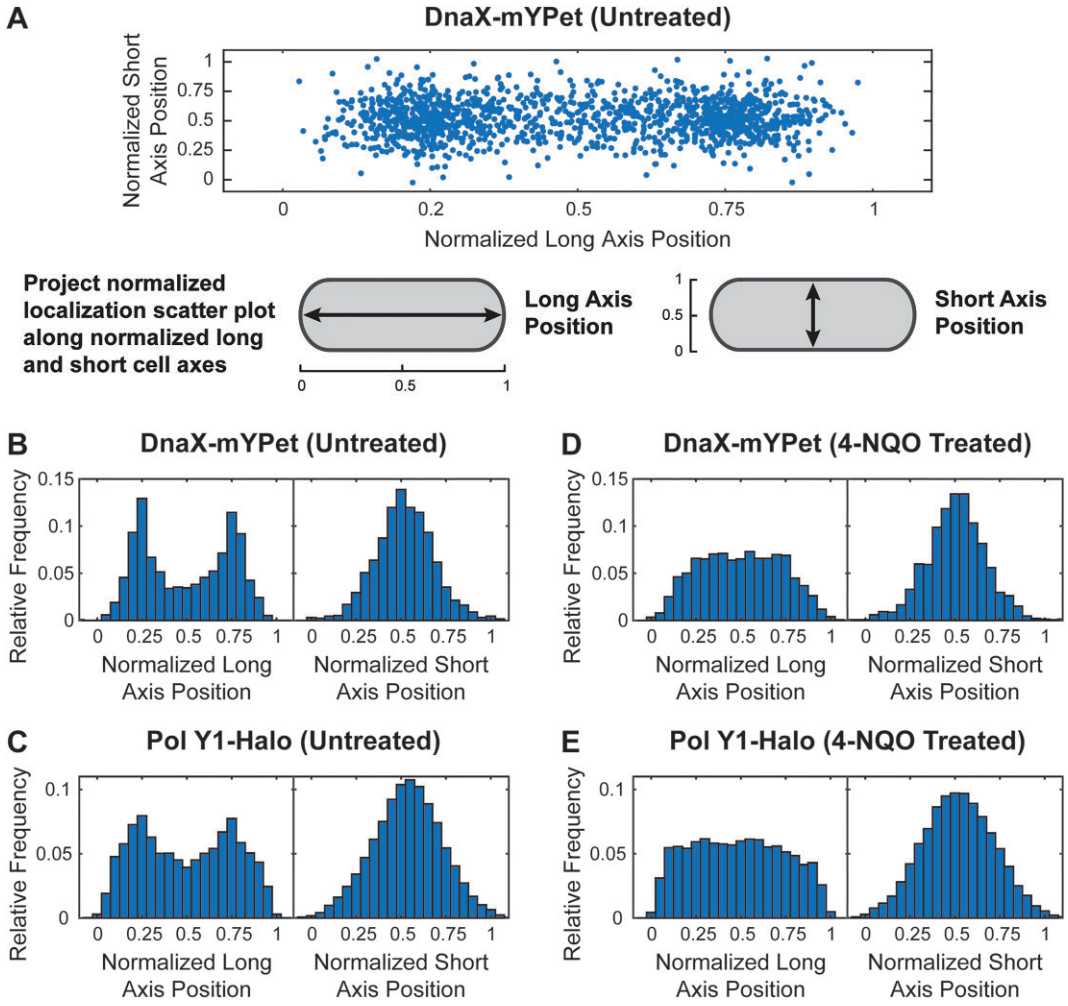

Figure 3. Cellular localization of DnaX-mYPet and Pol Y1-Halo. (**A**) Scatter plot of normalized positions of DnaX foci in untreated cells and cartoon of long and short cell axis projections. Plot and markers are scaled to reflect localization precision and average cell dimension. Long and short cell axis projections of (**B, D**) DnaX foci and (**C, E**) Pol Y1 trajectories in untreated cells and cells treated with 10 μM 4-NQO for 1 h, respectively.

firm that Pol Y1 molecules were associated with the nucleoid, as expected for a DNA polymerase, we used a strain bearing both Pol Y1-Halo and a C-terminal mYPet fusion to HBsu, a nucleoid-associated protein. HBsu binds non-specifically throughout the chromosome, and thus the intensity of the HBsu-mYPet signal reports on the DNA content (48). We quantified the average nucleoid intensity along the long axis of the cell and compared it to the average localization of Pol Y1. As expected, we found good agreement between Pol Y1 and nucleoid localization (Supplementary Figure S2E). Further, the short-axis localization pattern of Pol Y1, with a single peak at midcell (Figure 3C and Supplementary Figure S3C), indicates that Pol Y1 is not localized at the cell membrane, as was observed for *E. coli* Pol V (17). Although these results are aggregated across unsynchronized cell populations, taken together they suggest that Pol Y1 is enriched at or near sites of replication within the nucleoid region of the cell.

To assess intracellular colocalization more rigorously, we used radial distribution function analysis. In this approach, the radial distribution function, $g(r)$, represents the fold-enrichment of Pol Y1 molecules as a function of distance r from DnaX relative to random chance (Supplementary Figure S5A). A $g(r)$ value of one indicates no enrichment relative to chance, whereas higher values indicate greater colocalization (15,45). We observed moderate enrichment of Pol Y1 near DnaX, with a maximum $g(r) \approx 2.84$ (Figure 4A); again, the enrichment was similar when using longer 250 ms integration times (Supplementary Figure S5B). (See Supplementary Table S4 for quantification of variability in all $g(r)$ measurements.) In contrast, the *E. coli* homolog of Pol Y1, Pol IV, is only weakly enriched at sites of replication in the absence of DNA damage or other replication perturbations, with a maximum $g(r) \approx 1.5$ (14–16). This difference in degree of replication fork enrichment between Pol Y1 and Pol IV suggests differences in TLS polymerase regulation and activity between *B. subtilis* and *E. coli*.

There are static and mobile populations of Pol Y1 during normal growth

In *E. coli*, DNA polymerases exist in both static and mobile populations, characterized by slow and fast diffusion respectively (15,37). Next, we asked whether the same was true of Pol Y1 during normal growth. We quantified the motion of Pol Y1 by calculating an apparent diffusion coefficient, D^*, from the MSD of particle trajectories. The distribution of D^* values (Figure 5A) revealed a static population, with $D^* \approx 0$,

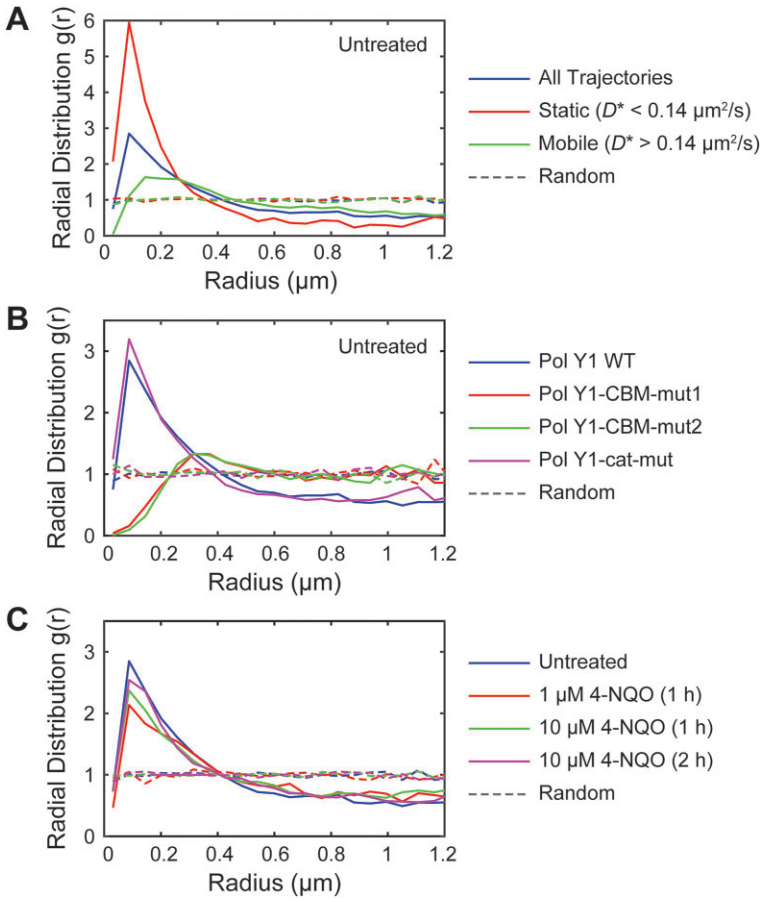

Figure 4. Radial distribution function $g(r)$ analysis of Pol Y1-Halo and DnaX-mYPet colocalization. (**A**) Pol Y1-DnaX $g(r)$ in untreated cells for all Pol Y1 trajectories, static Pol Y1 trajectories ($D^* < 0.14$ μm^2/s), and mobile Pol Y1 trajectories ($D^* > 0.14$ μm^2/s). (**B**) Pol Y1-DnaX $g(r)$ for WT Pol Y1, Pol Y1-CBM-mut1, Pol Y2-CBM-mut2 and Pol Y1-cat-mut in untreated cells. (**C**) Pol Y1-DnaX $g(r)$ in untreated cells and cells treated with 1 μM 4-NQO for 1 h, 10 μM 4-NQO for 1 h, or 10 μM 4-NQO for 2 h. Random $g(r)$ curves are shown as dashed lines. As described in the Methods section, $g(r) > 1$ indicates colocalization, whereas $g(r) = 1$ indicates no colocalization.

as well as a broad distribution of mobile molecules. To quantify these populations, we fit the D^* distribution to an analytical expression for three diffusing species; a two-population model did not fit the data well (Supplementary Figure S6J). We found that approximately 28% of Pol Y1 molecules were static ($D^* \approx 0.08$ μm^2/s). In addition, the fit revealed two mobile populations. The more highly mobile population ($D^* \approx 0.98$ μm^2/s) represented 47% of the population, whereas the intermediate population ($D^* \approx 0.23$ μm^2/s) represented 25%. (See Supplementary Table S5 for all diffusion coefficient distribution fit results.) The static population is immobilized through interactions with DNA, which diffuses very slowly in the cell, or with DNA-bound proteins; Pol Y1 molecules in this population may be, but are not necessarily, performing DNA synthesis. The more highly mobile population likely represents Pol Y1 molecules diffusing in the cytoplasm, whereas the intermediate population may represent transiently bound molecules.

To provide an alternative quantification of Pol Y1 mobility, we implemented the Spot-On algorithm, which fits a two-state model to the distribution of jump lengths (Supplementary Figure S7A). (See Supplementary Table S6 for all Spot-On analysis results for diffusion coefficients and population sizes.) In comparison to the MSD analysis, this approach revealed a larger bound population ($D^* \approx 0.02$ μm^2/s, ~40%). The diffusion coefficient of the mobile population ($D^* \approx 0.88$ μm^2/s, ~60%) was similar to that of the more highly mobile population in the three-state MSD analysis.

Next, we asked whether the static Pol Y1 population was preferentially enriched near sites of replication. To address this question, we compared the D^* distributions for Pol Y1 molecules less than or greater than 200 nm from a DnaX focus. We found that Pol Y1 molecules localized near DnaX foci were more likely to be static (Figure 5B), whereas molecules at greater distances were slightly more likely to be mobile (Figure 5C), with the static population reflecting approximately 44% and 24% of the total, respectively. Consistent with this analysis, we found a greater degree of Pol Y1-DnaX colocalization (maximum $g(r) \approx 5.95$) for static Pol Y1 molecules ($D^* < 0.14$ μm^2/s) (Figure 4A). Mobile Pol Y1 molecules ($D^* > 0.14$ μm^2/s) showed little to no colocalization at short r ($g(r) \approx 1.112$ at the peak r position characteristic of all trajectories), reaching a slightly higher but still low level of colocalization (maximum $g(r) \approx 1.633$) at slightly larger r values (Figure 4A). As observed for all Pol Y1 molecules, static Pol Y1 molecules were also localized within the same region of the cell as the nucleoid (Supplementary Figure S2F). Taken together, these results are consistent with recruitment and possible activity of Pol Y1 at or near sites of replication during normal replication.

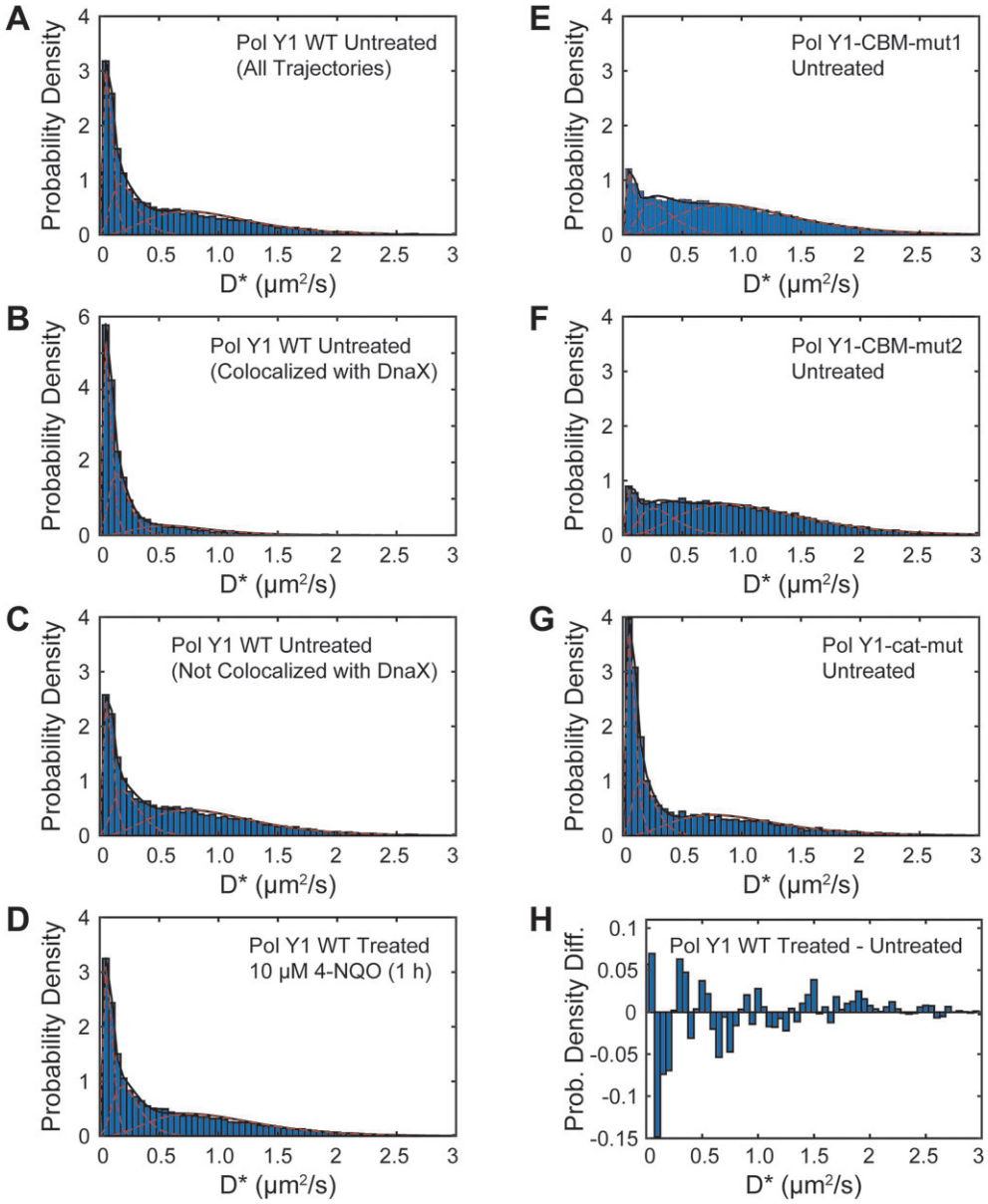

Figure 5. Apparent diffusion coefficient (D^*) distributions for Pol Y1-Halo, determined from trajectory MSD values as described in the Methods section, and corresponding three-population fits. D^* distributions for WT Pol Y1 in untreated cells for (**A**) all molecules, (**B**) molecules < 200 nm from DnaX-mYPet foci and (**C**) molecules > 200 nm from DnaX-mYPet foci. (**D**) D^* distributions for WT Pol Y1 in cells treated with 10 μM 4-NQO for 1 h. D^* distributions for (**E**) Pol Y1-CBM-mut1, (**F**) Pol Y1-CBM-mut2, and (**G**) Pol Y1-cat-mut mutants in untreated cells. (**H**) Difference between D^* distributions for WT Pol Y1 in 4-NQO-treated and untreated cells. Note different *y*-axis scales in panels (B) and (H).

The interaction with the DnaN clamp enriches Pol Y1 near sites of replication during normal growth

The activity of TLS polymerases in *E. coli* is mediated by critical protein-protein interactions with the β (DnaN) clamp; in particular, a strain bearing a Pol IV mutant unable to interact with the clamp is indistinguishable from a Pol IV knockout in damage tolerance (15,58). Pol Y1 contains a canonical CBM sequence (QLDLF) (Figure 1A) (19,23), like the *E. coli* TLS polymerases, but little is known about the functional role of the clamp interaction. To investigate the role of clamp-binding in Pol Y1 activity, we introduced two different sets of mutations to the CBM. The first, designated CBM-mut1 (QADAF), was previously shown to reduce untargeted mutagenesis by Pol Y1 (19). The second, designated CBM-mut2 (ALDLA), contains mutations to the highly conserved Gln and Phe residues, which are predicted to weaken clamp-binding substantially (23,59). To test the functional consequence of these mutations, we assayed 4-NQO survival as described previously. Both mutants were as sensitized to 4-NQO treatment as the Pol IV knockout (Figure 2C). Although these results do not prove a direct physical interaction between Pol Y1 and DnaN, they strongly suggest that such an interaction exists. Further, they indicate that the CBM sequence is critical for Pol Y1 activity in *B. subtilis*, like in *E. coli*.

Next, we investigated the effect of the clamp-binding mutations on the localization and dynamics of Pol Y1 during normal growth. In *E. coli*, the interaction with the clamp is essential for Pol IV activity (15,58,60), but the interaction with SSB plays a greater role in Pol IV enrichment near sites of replication (14,16). We constructed C-terminal HaloTag fu-

sions to both CBM mutants, in combination with the DnaX-mYPet replisome marker, and imaged cells under the same conditions as for WT Pol Y1. Radial distribution function analysis revealed a complete loss of Pol Y1-DnaX colocalization for both CBM mutants ($g(r) \approx 0.157$ and 0.0938 at short r values for Pol Y1-CBM-mut1 and Pol Y1-CBM-mut2, respectively) (Figure 4B). In contrast to WT Pol Y1, the $g(r)$ curves peaked at much larger r values, reaching ($g(r) \approx 1.3$ at $r > 300$ nm; similar behavior has been observed for two proteins that are localized in similar regions of the cell without being truly colocalized (15). This loss of colocalization with DnaX for the Pol Y1 CBM mutants is consistent with a reduction in their average localization at the long axis quarter and three-quarter positions (Supplementary Figures S4A and C). In contrast to changes in the long-axis localization of the Pol Y1 CBM mutants, however, their average short-axis localization remained centered at midcell, indicating that they were still broadly localized within the nucleoid region. Coupled with these changes in localization, there was a substantial reduction in the static population of Pol Y1 ($D^* \approx 0.08$ $\mu m^2/s$), from 28% for the Pol Y1 WT to 11% and 9% for Pol Y1-CBM-mut1 (Figure 5E) and Pol Y1-CBM-mut2 (Figure 5F), respectively. In qualitative agreement with this MSD diffusion analysis, Spot-On analysis revealed a greater than 50% reduction in the static population from approximately 40% for WT Pol Y1 to 19% and 17% for Pol Y1-CBM-mut1 (Supplementary Figure S7E) and Pol Y1-CBM-mut2 (Supplementary Figure S7F), respectively. Thus, the clamp interaction appears to play a major role in immobilizing and enriching Pol Y1 near sites of replication in *B. subtilis*, although these results do not exclude the possibility that other protein-protein interactions also contribute to Pol Y1 enrichment or activity.

Pol Y1 catalytic activity is not required for enrichment near sites of replication

Like other DNA polymerases, Pol Y1 contains conserved amino acids with negatively charged side chains that coordinate catalytic Mg^{2+} ions during DNA synthesis (61). To investigate the effect of Pol Y1 catalytic activity on its localization and dynamics *in vivo*, we introduced the catalytically inactivating D108 E109 → A108 A109 mutations (19). Pol Y1 catalytic activity was previously shown to be required for untargeted mutagenesis (19), but the effect on DNA damage tolerance has not been explored. First, we tested the survival of the Pol Y1-cat-mut catalytically inactive mutant in response to 4-NQO treatment. Like the clamp-binding mutants, the catalytic mutant was as sensitized to 4-NQO as the Pol Y1 knockout, indicating that catalytic activity is essential for damage tolerance (Figure 2C).

To look for any effects of catalytic activity on Pol Y1 localization and dynamics, we imaged cells with a Pol Y1-Halo fusion bearing the catalytic mutation during normal growth. In contrast to the results for the CBM mutants, radial distribution function analysis revealed a small increase in Pol Y1-DnaX enrichment for the catalytically inactive mutant relative to WT (maximum $g(r) \approx 3.20$) (Figure 4B), consistent with a similar average cellular localization pattern along both long and short cell axes (Supplementary Figure S4E). There was likewise a slight increase in the static population of Pol Y1 molecules ($D^* \approx 0.08$ $\mu m^2/s$), from 28% for Pol Y1 WT to 34% for Pol Y1-cat-mut (Figure 5G); diffusion analysis with the Spot-On algorithm was in qualitative agreement, with the static population increasing from approximately 40% for to 45% for the mutant (Supplementary Figure S7G). These results demonstrate that catalytic activity is not required to stabilize Pol Y1 near sites of replication. Instead, the modest increases in colocalization with sites of replication and in the static population is consistent with a picture in which Pol Y1-cat-mut spends more time bound near sites of replication due to its inability to perform DNA synthesis.

To compare the dynamics of the catalytically inactive mutant and WT Pol Y1 more carefully, we measured the binding lifetime for static Pol Y1 molecules imaged using a long 250 ms integration time. In this approach, the apparent binding lifetime is taken as the duration of the trajectory; when the Pol Y1 molecule dissociates from DNA or from a DNA-bound protein, the trajectory ends (Supplementary Figure S8A). However, photobleaching of the JFX_{554} fluorophore also terminates the trajectory and cannot be distinguished from a true dissociation event (Supplementary Figure S8A). To measure the JFX_{554} photobleaching rate under our imaging conditions, we imaged JFX_{554}-labeled WT Pol Y1 in fixed cells, where Pol Y1 is immobilized and there is no contribution from dissociation (15,37). Comparison of the apparent binding lifetime for WT Pol Y1 in untreated and fixed cells (Supplementary Figure S8B) revealed similar short-timescale dynamics, but a longer binding lifetime in fixed cells at longer timescales. In contrast, Pol Y1-cat-mut showed an intermediate binding lifetime at longer timescales, consistent with the small increase in the static population observed in diffusion coefficient measurements. To obtain photobleaching-corrected binding lifetime estimates, we first fit the apparent binding lifetime distributions to exponential functions (Supplementary Figures S8D–F and Supplementary Table S7). From the fit parameters, we extracted an effective photobleaching lifetime (1.10 ± 0.05 s) and photobleaching-corrected binding lifetimes for WT Pol Y1 (1.9 ± 0.4 s) and Pol Y1-cat-mut (6 ± 3 s), showing an approximately 3-fold increase in the binding lifetime for the catalytically inactive mutant relative to WT.

DNA damage leads to minimal changes in Pol Y1 localization and dynamics

In *E. coli*, the Pol Y1 homolog Pol IV is recruited to sites of replication in response to a variety of replication perturbations, including treatment with cognate DNA damaging agents, which generate DNA lesions that Pol IV can bypass efficiently (15,16). Given that Pol Y1 colocalizes with sites of replication during normal growth, we next asked whether this enrichment would increase upon DNA damage. To address this question, we chose to investigate the response of Pol Y1 to treatment with the drug 4-NQO; as shown previously, Pol Y1 promotes cell survival upon 4-NQO treatment.

First, we determined a 4-NQO treatment condition that would have a moderate effect on cell viability without being highly lethal. We tested exposure to a 1 μM 4-NQO concentration for 1 h in liquid culture and quantified the fold-change in the number of CFUs/ml (Supplementary Table S8). The number of CFUs/ml increased by a factor of 2.1 ± 0.2 (mean ± std.) after this treatment. In comparison, the number of CFUs/ml increased by 2.3 ± 0.6 in cells treated with the solvent DMF alone and by 2.09 ± 0.08 in untreated cells, indicating that this 4-NQO treatment had little or no effect on cell growth. We next tested higher concentrations of

10 and 50 μM with the same 1 h incubation time. For 10 μM, we observed a slight decrease in the number of CFUs/ml (fold change of 0.7 ± 0.2), whereas the 50 μM concentration produced a substantial decrease (fold change of 0.06 ± 0.02). Although these 4-NQO concentrations are one to two orders of magnitude greater than the concentrations used in the survival assays on solid media, it should be noted that the duration of treatment is much shorter (1 h in comparison to approximately 16 h).

In light of these results, we chose the 10 μM 4-NQO concentration as a starting point. We imaged cells after 1 h of treatment and quantified the localization and dynamics of Pol Y1. First, we looked at changes in the number and localization of DnaX foci. There was a small increase in the number of DnaX foci per cell (mean ± S.E.M.: 2.00 ± 0.04, $P < 10^{-5}$) in comparison to untreated cells. Although foci were still primarily localized between the quarter and three-quarter positions along the long cell axis, there was increased localization at midcell (Figure 3D and Supplementary Figure S3B). Similar behavior has been observed in *E. coli* and may reflect a slowdown in replication or a failure to initiate subsequent rounds of replication (15). Localization of DnaX foci remained peaked at midcell along the short axis, as in untreated cells. Notably, we observed analogous changes in Pol Y1 localization, with an increase in the fraction of Pol Y1 molecules at the midcell position along the long cell axis and no substantial change in the short-axis localization (Figure 3E and Supplementary Figure S3D). Consistent with these coupled changes in both DnaX and Pol Y1 localization, 4-NQO treatment had little effect on Pol Y1-DnaX colocalization. The radial distribution function showed moderate colocalization, with a slight reduction (maximum $g(r) \approx 2.370$) relative to untreated cells (Figure 4C).

In addition to the minimal changes in Pol Y1-DnaX localization, we also observed little change in Pol Y1 mobility upon 4-NQO treatment. The distribution of D^* values (Figure 5D) was comparable to that in untreated cells (Figure 5A), with approximately 28% of Pol Y1 molecules in the static ($D^* \approx 0.08$ μm^2/s) population; the change in the D^* distribution upon treatment is shown in Figure 5H. Consistent with the MSD diffusion analysis, Spot-On analysis indicated essentially no change in the static population upon DNA damage (Supplementary Figure S7C; ∼40% in untreated cells versus ∼41% in 4-NQO-treated cells). Likewise, we observed only a minimal change in the Pol Y1 binding lifetime upon 4-NQO treatment, with similar dynamics at both short and long timescales (Supplementary Figure S8C). Fitting the apparent binding lifetime distribution (Supplementary Figure S8G) yielded a photobleaching corrected binding lifetime of 2.2 ± 0.5 s, similar to the lifetime of 1.9 ± 0.4 s measured in untreated cells. Taken together, these results indicate that the dynamics of Pol Y1 do not change substantially under this 4-NQO treatment condition.

To explore a possible dose dependence in the response of Pol Y1 to 4-NQO DNA damage, we tested treatment with a lower 1 μM concentration for 1 h. As expected, we saw little effect on Pol Y1-DnaX colocalization (Figure 4C) or Pol Y1 mobility (Supplementary Figures S6E and S7B) for treatment with this lower concentration. Because cell viability was substantially reduced at higher 4-NQO concentrations, we did not test increased doses. Instead, we looked for possible delayed responses to treatment by exposing cells to 10 μM 4-NQO for a longer 2 h incubation, which slows cell growth but does not lead to a loss of viability (fold change of 1.5 ± 0.3 in the number of CFUs/ml). Again, we observed minimal changes in Pol Y1-DnaX colocalization (Figure 4C) or in the Pol Y1 diffusion coefficient (Supplementary Figures S6F and S7D) upon this treatment. In both cases, however, the average Pol Y1 localization pattern was closer to that in untreated cells (Supplementary Figures S3E and F). Thus, we were unable to find a 4-NQO treatment condition that led to substantial recruitment of Pol Y1 to sites of replication, as observed for *E. coli* Pol IV, or to substantial changes in Pol Y1 dynamics.

In addition to characterizing the response of WT Pol Y1 to 4-NQO treatment, we also determined the response of the clamp-binding and catalytically inactive mutants. Overall, the mutant Pol Y1 localization (Supplementary Figures S4B, D and F), colocalization with sites of replication (Supplementary Figure S5C), and diffusion (Supplementary Figures S6G–I and Supplementary Figures S7H–J) were consistent with the observed behavior for each mutant in untreated cells. The catalytically inactive mutant, Pol Y1-catmut, showed modest increases in colocalization with sites of replication (Supplementary Figure S5C) and in the fraction of static molecules (Supplementary Figures S6I and S7J) relative to WT Pol Y1. In contrast, the clamp-binding mutants, Pol Y1-CBM-mut1 and Pol Y1-CBM-mut2, were not colocalized with sites of replication (Supplementary Figure S5C) and had substantial reductions in the static Pol Y1 population (Supplementary Figures S6G and H and S7H and I). Thus, 4-NQO treatment does not appear to alter the molecular requirements for Pol Y1 enrichment and stabilization at sites of replication; the clamp-binding interaction is still required, but catalytic activity is not.

Pol Y1 has little impact on spontaneous or 4-NQO-induced mutagenesis

Taken together, our results indicate that Pol Y1 is present near sites of replication both during normal growth and upon DNA damage induced by 4-NQO, and that it promotes cell survival in the presence of 4-NQO. In *E. coli*, Pol IV has no measurable effect on the rate of spontaneous mutations (62), but it contributes to mutagenesis upon DNA damage, including by 4-NQO (63). Thus, we asked whether the same was true of Pol Y1. As a proxy for the overall mutation rate, we measured the fraction of cells that developed resistance to the drug rifampicin at 10 μg/ml concentration; rifampicin resistance (Rif^R) is generally conferred by mutations to the RNA polymerase β-subunit, encoded by the gene *rpoB* (64,65). Consistent with prior studies in *B. subtilis* (19,33), we found that the spontaneous Rif^R rate was on the order of one per 10^8 cells for the untreated WT strain (Figure 6 and Supplementary Table S9). Spontaneous mutation rates for the Pol Y1 and Pol Y2 knockout strains were essentially identical to WT in untreated cells. To quantify 4-NQO damage-induced mutagenesis, we treated cells with a 10 μM concentration of 4-NQO for 1 h, the same condition used for microscopy. The Rif^R rates for each strain were modestly higher (at most a 50% increase) upon 4-NQO treatment, although this difference was only statistically significant ($P < 0.05$) for the Pol Y2 knockout strain. As for spontaneous mutagenesis, there was no statistically significant difference in the Rif^R rates between strains upon 4-NQO treatment. Finally, we calculated the induced mutation rate as the difference be-

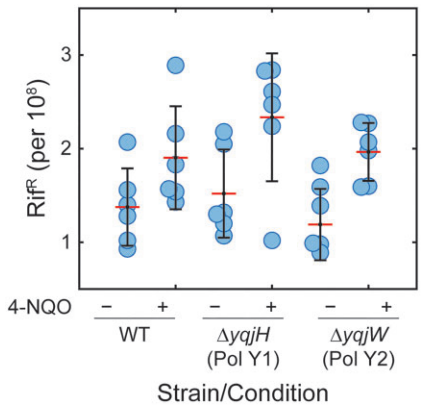

Figure 6. Effect of Pol Y1 and Pol Y2 on spontaneous and 4-NQO-induced mutagenesis. Proportion of rifampicin resistant (Rif^R) cells for WT and Pol Y1 and Pol Y2 knockout strains, either untreated or treated with 10 μM 4-NQO for 1 h. For each dataset, the individual replicates are shown as circles, the red line represents the mean value, and the error bars represent the standard deviation.

tween the mutation rate in 4-NQO-treated and untreated cells (Supplementary Table S9). Differences in the induced mutation rate, which ranged from 0.5 to 1.0 per 10^8 cells, were not statistically significant between strains. Therefore, despite the role of Pol Y1 in promoting survival to 4-NQO treatment, it does not appear to play a significant role in mutagenesis, at least under these conditions.

Discussion

Y-family DNA polymerases and the TLS pathway are conserved across a wide range of bacterial species, yet most previous work has focused on the model gram-negative bacterium *E. coli*. (3) In this study, we used single-molecule fluorescence microscopy to characterize the localization and dynamics of the TLS polymerase Pol Y1, a homolog of *E. coli* Pol IV, in the gram-positive bacterium *B. subtilis*. We created a new functional HaloTag fusion to the endogenous copy of Pol Y1 and used quantitative fluorescence microscopy and single-particle tracking to determine its dynamics and localization at the single-molecule level in live cells, both in the absence of exogenous DNA damage and upon treatment with the drug 4-NQO.

Given the low fidelity and slow rate of synthesis of most TLS polymerases, their access to the DNA template during normal replication can be harmful (66). Although TLS polymerases promote mutagenesis if overexpressed (19,67), in *E. coli* they make little contribution to the basal mutation rate at normal expression levels (62). An emerging model suggests an explanation for these observations in terms of a spatial component to the regulation of TLS polymerases in *E. coli*; in this model, TLS polymerases are restricted from the replication fork during normal growth and only enriched, if at all, upon perturbations to replication (Figure 7, top panels) (11,14–17). In contrast, we found that *B. subtilis* Pol Y1 is moderately enriched at or near sites of replication during normal growth (Figure 7, bottom left panel). By measuring the diffusion of Pol Y1 molecules, we showed that the static Pol Y1 population is particularly enriched at these sites, suggesting that Pol Y1 is interacting either with DNA or with other DNA-bound proteins at or near the replication fork. Unlike *E. coli* TLS polymerases, Pol Y1 is not upregulated by the SOS DNA damage response (19,22). Taken together with our imaging results, this observation supports the possibility that Pol Y1 is playing a role in normal replication, possibly in alleviating replication-transcription conflicts or in the transcription-coupled NER pathway (26). Notably, the transcription/repair coupling factor Mfd is found to be associated with the nucleoid even in the absence of exogenous DNA damage in *E. coli* (68). More broadly, these results indicate that there are different patterns of spatial regulation of TLS polymerases across different bacterial species and suggest that studies in other species may reveal different mechanisms.

In *E. coli*, changes in the localization and dynamics of TLS polymerases have been observed upon DNA damage or other perturbations to replication; in particular, Pol IV is strongly recruited to sites of replication upon induction of DNA damage by methyl methanesulfonate (MMS) or ultraviolet (UV) light (Figure 7, top right panel) (16). In this study, we characterized the localization and dynamics of Pol Y1 after different treatments with the drug 4-NQO; consistent with previous work (26), we found that Pol Y1, but not Pol Y2, mediates cell survival to 4-NQO treatment. Surprisingly, we observed little or no change in Pol Y1 behavior, including its colocalization with sites of replication and its dynamics, upon 4-NQO treatment (Figure 7, bottom right panel). In contrast to Pol IV, Pol Y1 is not transcriptionally upregulated by the SOS DNA damage response (19,22). Although SOS induction of Pol IV plays an important role in its response to DNA damage, selective recruitment of Pol IV to the replication fork upon replication stalling was observed in a constitutively SOS-induced strain where Pol IV levels were unchanged upon DNA damage (15,16). Thus, the lack of SOS induction of Pol Y1 is likely not sufficient to explain the lack of response to 4-NQO treatment. These results raise the possibility that Pol Y1 promotes cell survival upon DNA damage through different mechanisms than Pol IV.

Like replicative DNA polymerases, TLS polymerases function with the assistance of accessory proteins. In *E. coli*, the interaction between TLS polymerases and the replication processivity factor, the sliding clamp, is essential for TLS (3,58,60). Recent single-molecule imaging experiments have revealed that the clamp interaction contributes to the enrichment of Pol IV at sites of replication upon DNA damage (15). However, interactions with another replication protein, SSB, are the primary driver for Pol IV localization (Figure 7, top right panel) (14). Like Pol IV, Pol Y1 contains a conserved CBM, suggesting that it interacts with the DnaN clamp (19); indirect evidence for this interaction has also been provided by a yeast two-hybrid screen (24). We characterized two Pol Y1 mutants with modifications to its CBM that are predicted to eliminate clamp binding and found that both mutants were as sensitive to treatment with 4-NQO as was a Pol Y1 knockout, indicating that the clamp interaction is critical for Pol Y1-mediated damage tolerance. These results are consistent with the sensitization of Pol IV-CBM mutants in *E. coli* (58), where a direct physical interaction between Pol IV and DnaN has been established (69). Further, single-molecule imaging of these CBM mutants revealed a reduction in the static population of Pol Y1 and a loss of Pol Y1-DnaX colocalization, both during normal growth and upon 4-NQO treatment. Taken together, these results strongly suggest that Pol Y1 is interacting with DNA-bound clamps at or near the replication fork (Figure 7, bottom panels), but they do not exclude

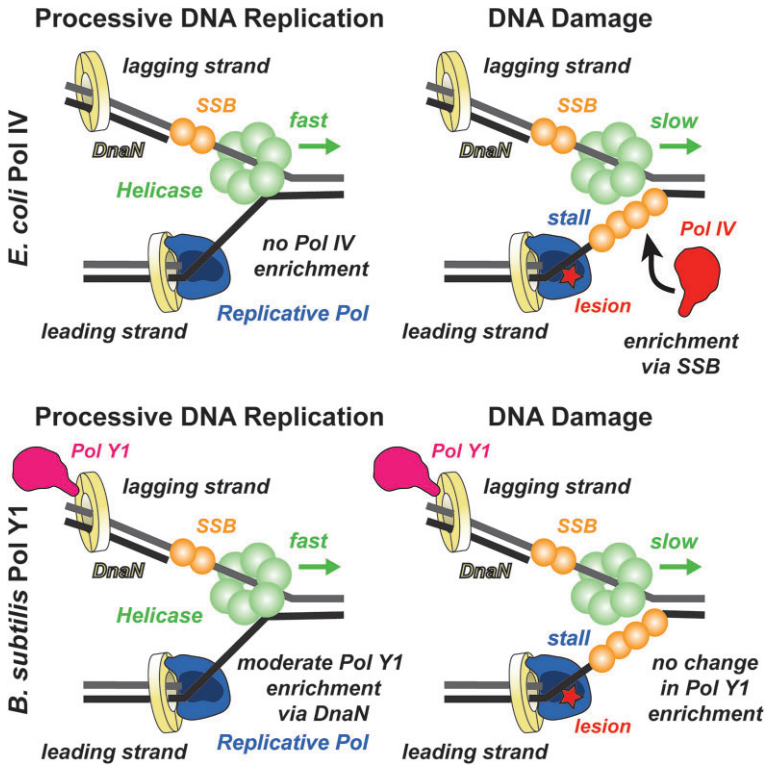

Figure 7. Model of different TLS polymerase recruitment mechanisms in *E. coli* and *B. subtilis*. In *E. coli*, there is little or no enrichment of Pol IV near the replication fork during processive replication (*top left*), but a significant increase in enrichment upon DNA damage-induced replication stalling, primarily through interactions with SSB (*top right*). In *B. subtilis*, Pol Y1 is moderately enriched near the replication fork through interactions with DnaN, both during processive replication (*bottom left)* and upon DNA damage-induced replication stalling (*bottom right*).

the possibility that other protein-protein interactions, particularly with SSB, play a role in Pol Y1 activity.

We also investigated the effect of Pol Y1 catalytic activity on its localization and dynamics. In *E. coli*, imaging studies of Pol IV have reached different conclusions about the role of catalytic activity in localization; one found a complete loss of Pol IV foci upon DNA damage for a catalytically inactive mutant (11), whereas another found only a modest decrease in Pol IV colocalization with sites of replication (15). Here, we observed that a catalytically inactive Pol Y1 mutant, although broadly similar to WT Pol Y1 in its behavior, showed several hallmarks of increased stability at sites of replication. Although the changes were modest, Pol Y1-cat-mut had greater enrichment at sites of replication relative to WT Pol Y1 and a larger static population in diffusion coefficient measurements, both during normal growth and upon 4-NQO treatment. Likewise, there was an increase in the binding lifetime of static Pol Y1-cat-mut molecules relative to WT during normal growth. These results support a picture where stabilization of Pol Y1 near the replication fork does not require DNA synthesis.

In *E. coli*, Pol IV contributes to mutagenesis upon DNA damage or when overexpressed (63), but it does not increase the mutation rate at normal expression levels in the absence of damage (62). Prior work has explored the effect of Pol Y1 on both spontaneous and damage-induced mutagenesis, with some conflicting results. Consistent with our findings, two studies reported little or no effect of Pol Y1 on the spontaneous mutation rate (18,19). However, one study found that Pol Y1 contributed to UV-induced mutagenesis (18), whereas the other did not (19). There is also evidence that Pol Y1 promotes lagging-strand mutagenesis when replication-transcription conflicts are induced at specific loci (26). Although further work is needed to determine the effect of Pol Y1 on mutagenesis under different conditions, the minimal effect of Pol Y1 on spontaneous or 4-NQO-induced mutagenesis is somewhat surprising given our findings that Pol Y1 is constitutively enriched near replication forks through its interaction with the DnaN clamp and may suggest that other mechanisms limit the access of Pol Y1 to the template.

Taken together, our results show that there are significant differences in the activity of *B. subtilis* Pol Y1 in comparison to its *E. coli* homolog Pol IV (Figure 7). This work is the first step toward elucidating the mechanisms of TLS polymerases in *B. subtilis* at the single-molecule level, but many key questions remain. First, is the lack of damage-induced Pol Y1 enrichment at sites of replication unique to 4-NQO treatment, or is it common to all types of DNA damage? Although beyond the scope of this work, future studies should explore the response of Pol Y1 to different types of replication perturbations, including diverse forms of DNA damage. Second, what other protein-protein interactions, if any, play a role in Pol Y1 activity? We have shown that the interaction with the DnaN clamp is essential to 4-NQO damage tolerance and drives Pol Y1 localization and dynamics *in vivo*. Although at least 12 SSB-interacting proteins have been identified in *B. subtilis*, Pol Y1 is not among them (20,70). By analogy to the *E. coli* TLS polymerases, however, the possibility of an interaction with SSB should be explored. Additionally, there is experimental or computational evidence for interactions with RecA (25) and Pol I (24) that merit further investigation. Finally, what are the primary cellular functions of Pol Y1? Its lack of SOS induction

and constitutive enrichment near sites of replication suggest that it may have an important role beyond replication-coupled TLS. In particular, future studies should explore Pol Y1 involvement in resolving replication-transcription conflicts, including a possible role in the transcription-coupled NER pathway. Answering these and other questions about TLS polymerase activity in *B. subtilis* will help broaden bacterial models for TLS beyond *E. coli* and provide new insight into how cells maintain a balance between genome stability and mutagenesis under stress.

Data availability

Data and custom MATLAB code from this study are available in the Zenodo repository (DOI: 10.5281/zenodo.11977908).

Supplementary data

Supplementary Data are available at NAR Online.

Acknowledgements

We thank Xindan Wang (Indiana University) for sharing several bacterial strains and for advice in strain construction, Joseph Loparo (Harvard Medical School) for sharing bacterial strains, and Luke Lavis (Howard Hughes Medical Institute Janelia Research Campus) for providing Janelia Fluor dyes. We also acknowledge Nicholas Bafundo for contributions to the strain construction strategy and Emily Holmes, Luke O'Neal and Sophia Martinez-Whitman for assistance with microscopy.

Funding

National Institute of General Medical Sciences of the National Institutes of Health [R15GM151677 to E.S.T.]; National Science Foundation [1833931 providing support to A.S.J., C.R.G.]; Fordham College at Rose Hill Undergraduate Research Grant program [to M.E.M., M.R.F., Y.C., M.N.D.]; Fordham University Clare Boothe Luce program [to M.E.M., C.M.S.]; Fordham University Len Blavatnik STEM Fellowship [to M.E.M., M.R.F.]. Funding for open access charge: Internal Fordham University research funds and National Institutes of Health [R15GM151677].

Conflict of interest statement

None declared.

References

1. Johnson,A. and O'Donnell,M. (2005) Cellular DNA replicases: components and dynamics at the replication fork. *Annu. Rev. Biochem.*, **74**, 283–315.
2. Fuchs,R.P. and Fujii,S. (2013) Translesion DNA synthesis and mutagenesis in prokaryotes. *Cold Spring Harb. Perspect. Biol.*, **5**, a012682.
3. Fujii,S. and Fuchs,R.P. (2020) A comprehensive view of translesion synthesis in Escherichia coli. *Microbiol. Mol. Biol. Rev.*, **84**, e00002-20.
4. Joseph,A.M. and Badrinarayanan,A. (2020) Visualizing mutagenic repair: novel insights into bacterial translesion synthesis. *FEMS Microbiol. Rev.*, **44**, 572–582.
5. Sale,J.E., Lehmann,A.R. and Woodgate,R. (2012) Y-family DNA polymerases and their role in tolerance of cellular DNA damage. *Nat. Rev. Mol. Cell Biol.*, **13**, 141–152.
6. Goodman,M.F. and Woodgate,R. (2013) Translesion DNA polymerases. *Cold Spring Harb. Perspect. Biol.*, **5**, a010363.
7. Paz-Elizur,T., Takeshita,M., Goodman,M., O'Donnell,M. and Livneh,Z. (1996) Mechanism of translesion DNA synthesis by DNA polymerase II. *J. Biol. Chem.*, **271**, 24662–24669.
8. Becherel,O.J. and Fuchs,R.P.P. (2001) Mechanism of DNA polymerase II-mediated frameshift mutagenesis. *Proc. Natl. Acad. Sci. U.S.A.*, **98**, 8566–8571.
9. Simmons,L.A., Foti,J.J., Cohen,S.E. and Walker,G.C. (2008) The SOS regulatory network. *EcoSal Plus*, **2008**, https://doi.org/10.1128/ecosalplus.5.4.3.
10. Sutton,M.D. (2010) Coordinating DNA polymerase traffic during high and low fidelity synthesis. *Biochim. Biophys. Acta Proteins Proteom.*, **1804**, 1167–1179.
11. Henrikus,S.S., Wood,E.A., McDonald,J.P., Cox,M.M., Woodgate,R., Goodman,M.F., van Oijen,A.M. and Robinson,A. (2018) DNA polymerase IV primarily operates outside of DNA replication forks in Escherichia coli. *PLoS Genet.*, **14**, e1007161.
12. Bonner,C.A., Stukenberg,P.T., Rajagopalan,M., Eritja,R., O'Donnell,M., McEntee,K., Echols,H. and Goodman,M.F. (1992) Processive DNA synthesis by DNA polymerase II mediated by DNA polymerase III accessory proteins. *J. Biol. Chem.*, **267**, 11431–11438.
13. Shereda,R.D., Kozlov,A.G., Lohman,T.M., Cox,M.M. and Keck,J.L. (2008) SSB as an organizer/mobilizer of genome maintenance complexes. *Crit. Rev. Biochem. Mol. Biol.*, **43**, 289–318.
14. Chang,S., Thrall,E.S., Laureti,L., Piatt,S.C., Pagès,V. and Loparo,J.J. (2022) Compartmentalization of the replication fork by single-stranded DNA-binding protein regulates translesion synthesis. *Nat. Struct. Mol. Biol.*, **29**, 932–941.
15. Thrall,E.S., Kath,J.E., Chang,S. and Loparo,J.J. (2017) Single-molecule imaging reveals multiple pathways for the recruitment of translesion polymerases after DNA damage. *Nat. Commun.*, **8**, 2170.
16. Thrall,E.S., Piatt,S.C., Chang,S. and Loparo,J.J. (2022) Replication stalling activates SSB for recruitment of DNA damage tolerance factors. *Proc. Natl. Acad. Sci. U.S.A.*, **119**, e2208875119.
17. Robinson,A., McDonald,J.P., Caldas,V.E.A., Patel,M., Wood,E.A., Punter,C.M., Ghodke,H., Cox,M.M., Woodgate,R., Goodman,M.F., *et al.* (2015) Regulation of mutagenic DNA polymerase V activation in space and time. *PLoS Genet.*, **11**, e1005482.
18. Sung,H.-M., Yeamans,G., Ross,C.A. and Yasbin,R.E. (2003) Roles of YqjH and YqjW, homologs of the escherichiacoli UmuC/DinB or Y superfamily of DNA polymerases, in stationary-phase mutagenesis and UV-induced mutagenesis of Bacillus subtilis. *J. Bacteriol.*, **185**, 2153–2160.
19. Duigou,S., Ehrlich,S.D., Noirot,P. and Noirot-Gros,M.-F. (2004) Distinctive genetic features exhibited by the Y-family DNA polymerases in Bacillus subtilis. *Mol. Microbiol.*, **54**, 439–451.
20. Lenhart,J.S., Schroeder,J.W., Walsh,B.W. and Simmons,L.A. (2012) DNA repair and genome maintenance in Bacillus subtilis. *Microbiol. Mol. Biol. Rev.*, **76**, 530–564.
21. Permina,E.A., Mironov,A.A. and Gelfand,M.S. (2002) Damage-repair error-prone polymerases of eubacteria: association with mobile genome elements. *Gene*, **293**, 133–140.
22. Au,N., Kuester-Schoeck,E., Mandava,V., Bothwell,L.E., Canny,S.P., Chachu,K., Colavito,S.A., Fuller,S.N., Groban,E.S., Hensley,L.A., *et al.* (2005) Genetic composition of the Bacillus subtilis SOS system. *J. Bacteriol.*, **187**, 7655–7666.
23. Dalrymple,B.P., Kongsuwan,K., Wijffels,G., Dixon,N.E. and Jennings,P.A. (2001) A universal protein–protein interaction motif in the eubacterial DNA replication and repair systems. *Proc. Natl. Acad. Sci. U.S.A.*, **98**, 11627–11632.

24. Duigou,S., Ehrlich,S.D., Noirot,P. and Noirot-Gros,M.-F. (2005) DNA polymerase I acts in translesion synthesis mediated by the Y-polymerases in Bacillus subtilis. *Mol. Microbiol.*, **57**, 678–690.
25. Timinskas,K. and Venclovas,Č. (2019) New insights into the structures and interactions of bacterial Y-family DNA polymerases. *Nucleic Acids Res.*, **47**, 4393–4405.
26. Million-Weaver,S., Samadpour,A.N., Moreno-Habel,D.A., Nugent,P., Brittnacher,M.J., Weiss,E., Hayden,H.S., Miller,S.I., Liachko,I. and Merrikh,H. (2015) An underlying mechanism for the increased mutagenesis of lagging-strand genes in *Bacillus subtilis*. *Proc. Natl. Acad. Sci. U.S.A.*, **112**, E1096–E1105.
27. Courcelle,C.T., Belle,J.J. and Courcelle,J. (2005) Nucleotide excision repair or polymerase V-mediated lesion bypass can act to restore UV-arrested replication forks in Escherichia coli. *J. Bacteriol.*, **187**, 6953–6961.
28. Cohen,S.E., Godoy,V.G. and Walker,G.C. (2009) Transcriptional modulator NusA interacts with translesion DNA polymerases in Escherichia coli. *J. Bacteriol.*, **191**, 665–672.
29. Cohen,S.E., Lewis,C.A., Mooney,R.A., Kohanski,M.A., Collins,J.J., Landick,R. and Walker,G.C. (2010) Roles for the transcription elongation factor NusA in both DNA repair and damage tolerance pathways in Escherichia coli. *Proc. Natl. Acad. Sci. U.S.A.*, **107**, 15517–15522.
30. Zeigler,D.R., Prágai,Z., Rodriguez,S., Chevreux,B., Muffler,A., Albert,T., Bai,R., Wyss,M. and Perkins,J.B. (2008) The origins of 168, W23, and other *Bacillus subtilis* legacy strains. *J. Bacteriol.*, **190**, 6983–6995.
31. Schroeder,J.W. and Simmons,L.A. (2013) Complete genome sequence of Bacillus subtilis strain PY79. *Genome Announc.*, **1**, e01085-13.
32. Gibson,D.G., Young,L., Chuang,R.-Y., Venter,J.C., Hutchison,C.A. and Smith,H.O. (2009) Enzymatic assembly of DNA molecules up to several hundred kilobases. *Nat. Methods*, **6**, 343–345.
33. Le Chatelier,E., Bécherel,O.J., d'Alençon,E., Canceill,D., Ehrlich,S.D., Fuchs,R.P.P. and Jannière,L. (2004) Involvement of DnaE, the second replicative DNA polymerase from Bacillus subtilis, in DNA Mutagenesis. *J. Biol. Chem.*, **279**, 1757–1767.
34. Grossman,A.D. and Losick,R. (1988) Extracellular control of spore formation in Bacillus subtilis. *Proc. Natl. Acad. Sci. U.S.A.*, **85**, 4369–4373.
35. Grimm,J.B., Xie,L., Casler,J.C., Patel,R., Tkachuk,A.N., Falco,N., Choi,H., Lippincott-Schwartz,J., Brown,T.A., Glick,B.S., *et al.* (2021) A general method to improve fluorophores using deuterated auxochromes. *JACS Au*, **1**, 690–696.
36. Los,G.V., Encell,L.P., McDougall,M.G., Hartzell,D.D., Karassina,N., Zimprich,C., Wood,M.G., Learish,R., Ohana,R.F., Urh,M., *et al.* (2008) HaloTag: a novel protein labeling technology for cell imaging and protein analysis. *ACS Chem. Biol.*, **3**, 373–382.
37. Uphoff,S., Reyes-Lamothe,R., Garza De Leon,F., Sherratt,D.J. and Kapanidis,A.N. (2013) Single-molecule DNA repair in live bacteria. *Proc. Natl. Acad. Sci. U.S.A.*, **110**, 8063–8068.
38. Bisson-Filho,A.W., Hsu,Y.-P., Squyres,G.R., Kuru,E., Wu,F., Jukes,C., Sun,Y., Dekker,C., Holden,S., VanNieuwenhze,M.S., *et al.* (2017) Treadmilling by FtsZ filaments drives peptidoglycan synthesis and bacterial cell division. *Science*, **355**, 739–743.
39. Tokunaga,M., Imamoto,N. and Sakata-Sogawa,K. (2008) Highly inclined thin illumination enables clear single-molecule imaging in cells. *Nat. Methods*, **5**, 159–161.
40. Sliusarenko,O., Heinritz,J., Emonet,T. and Jacobs-Wagner,C. (2011) High-throughput, subpixel precision analysis of bacterial morphogenesis and intracellular spatio-temporal dynamics: quantitative analysis of spatio-temporal dynamics. *Mol. Microbiol.*, **80**, 612–627.
41. Jaqaman,K., Loerke,D., Mettlen,M., Kuwata,H., Grinstein,S., Schmid,S.L. and Danuser,G. (2008) Robust single-particle tracking in live-cell time-lapse sequences. *Nat. Methods*, **5**, 695–702.
42. Aguet,F., Antonescu,C.N., Mettlen,M., Schmid,S.L. and Danuser,G. (2013) Advances in analysis of low signal-to-noise images link dynamin and AP2 to the functions of an endocytic checkpoint. *Dev. Cell*, **26**, 279–291.
43. Stracy,M., Lesterlin,C., Garza de Leon,F., Uphoff,S., Zawadzki,P. and Kapanidis,A.N. (2015) Live-cell superresolution microscopy reveals the organization of RNA polymerase in the bacterial nucleoid. *Proc. Natl. Acad. Sci. U.S.A.*, **112**, E4390–E4399.
44. Hansen,A.S., Woringer,M., Grimm,J.B., Lavis,L.D., Tjian,R. and Darzacq,X. (2018) Robust model-based analysis of single-particle tracking experiments with Spot-On. *eLife*, **7**, e33125.
45. Zawadzki,P., Stracy,M., Ginda,K., Zawadzka,K., Lesterlin,C., Kapanidis,A.N. and Sherratt,D.J. (2015) The localization and action of topoisomerase IV in Escherichia coli chromosome segregation is coordinated by the SMC complex, MukBEF. *Cell Rep.*, **13**, 2587–2596.
46. Garza de Leon,F., Sellars,L., Stracy,M., Busby,S.J.W. and Kapanidis,A.N. (2017) Tracking low-copy transcription factors in living bacteria: the case of the lac repressor. *Biophys. J.*, **112**, 1316–1327.
47. Nguyen,A.W. and Daugherty,P.S. (2005) Evolutionary optimization of fluorescent proteins for intracellular FRET. *Nat. Biotechnol.*, **23**, 355–360.
48. Wang,X., Montero Llopis,P. and Rudner,D.Z. (2014) *Bacillus subtilis* chromosome organization oscillates between two distinct patterns. *Proc. Natl. Acad. Sci. U.S.A.*, **111**, 12877–12882.
49. Liao,Y., Schroeder,J.W., Gao,B., Simmons,L.A. and Biteen,J.S. (2015) Single-molecule motions and interactions in live cells reveal target search dynamics in mismatch repair. *Proc. Natl. Acad. Sci. U.S.A.*, **112**, E6698–E6906.
50. Mangiameli,S.M., Veit,B.T., Merrikh,H. and Wiggins,P.A. (2017) The replisomes remain spatially proximal throughout the cell cycle in bacteria. *PLoS Genet.*, **13**, e1006582.
51. Hernández-Tamayo,R., Oviedo-Bocanegra,L.M., Fritz,G. and Graumann,P.L. (2019) Symmetric activity of DNA polymerases at and recruitment of exonuclease ExoR and of PolA to the Bacillus subtilis replication forks. *Nucleic Acids Res.*, **47**, 8521–8536.
52. Tuson,H.H., Aliaj,A., Brandes,E.R., Simmons,L.A. and Biteen,J.S. (2016) Addressing the requirements of high-sensitivity single-molecule imaging of low-copy-number proteins in bacteria. *ChemPhysChem*, **17**, 1435–1440.
53. Menichini,P., Fronza,G., Tornaletti,S., Galiègue-Zouitina,S., Bailleul,B., Loucheux-Lefebvre,M.H., Abbondandolo,A. and Pedrini,A.M. (1989) In vitro DNA modification by the ultimate carcinogen of 4-nitroquinoline-1-oxide: influence of superhelicity. *Carcinogenesis*, **10**, 1589–1593.
54. Fronza,G., Campomenosi,P., Iannone,R. and Abbondandolo,A. (1992) The 4-nitroquinoline 1-oxide mutational spectrum in single stranded DNA is characterized by guanine to pyrimidine transversions. *Nucleic Acids Res.*, **20**, 1283–1287.
55. Williams,A.B., Hetrick,K.M. and Foster,P.L. (2010) Interplay of DNA repair, homologous recombination, and DNA polymerases in resistance to the DNA damaging agent 4-nitroquinoline-1-oxide in Escherichia coli. *DNA Repair (Amst.)*, **9**, 1090–1097.
56. Gurskaya,N.G., Verkhusha,V.V., Shcheglov,A.S., Staroverov,D.B., Chepurnykh,T.V., Fradkov,A.F., Lukyanov,S. and Lukyanov,K.A. (2006) Engineering of a monomeric green-to-red photoactivatable fluorescent protein induced by blue light. *Nat. Biotechnol.*, **24**, 461–465.
57. Chudakov,D.M., Lukyanov,S. and Lukyanov,K.A. (2007) Tracking intracellular protein movements using photoswitchable fluorescent proteins PS-CFP2 and Dendra2. *Nat. Protoc.*, **2**, 2024–2032.
58. Becherel,O.J., Fuchs,R.P.P. and Wagner,J. (2002) Pivotal role of the β-clamp in translesion DNA synthesis and mutagenesis in E. coli cells. *DNA Repair (Amst.)*, **1**, 703–708.
59. Wijffels,G., Dalrymple,B.P., Prosselkov,P., Kongsuwan,K., Epa,V.C., Lilley,P.E., Jergic,S., Buchardt,J., Brown,S.E., Alewood,P.F., *et al.* (2004) Inhibition of protein interactions with the β_2 clamp of Escherichia coli DNA polymerase III by peptides from β_2-binding proteins. *Biochemistry*, **43**, 5661–5671.

60. Wagner,J., Fujii,S., Gruz,P., Nohmi,T. and Fuchs,R.P.P. (2000) The β clamp targets DNA polymerase IV to DNA and strongly increases its processivity. *EMBO Rep.*, **1**, 484–488.
61. Rothwell,P.J. and Waksman,G. (2005) Structure and mechanism of DNA polymerases. *Adv. Protein Chem.*, **71**, 401–440.
62. Kuban,W., Jonczyk,P., Gawel,D., Malanowska,K., Schaaper,R.M. and Fijalkowska,I.J. (2004) Role of *Escherichia coli* DNA polymerase IV in In vivo replication fidelity. *J. Bacteriol.*, **186**, 4802–4807.
63. Kim,S.-R., Matsui,K., Yamada,M., Gruz,P. and Nohmi,T. (2001) Roles of chromosomal and episomal dinB genes encoding DNA pol IV in targeted and untargeted mutagenesis in Escherichia coli. *Mol Gen Genomics*, **266**, 207–215.
64. Campbell,E.A., Korzheva,N., Mustaev,A., Murakami,K., Nair,S., Goldfarb,A. and Darst,S.A. (2001) Structural mechanism for rifampicin inhibition of bacterial RNA polymerase. *Cell*, **104**, 901–912.
65. Goldstein,B.P. (2014) Resistance to rifampicin: a review. *J. Antibiot.*, **67**, 625–630.
66. Uchida,K., Furukohri,A., Shinozaki,Y., Mori,T., Ogawara,D., Kanaya,S., Nohmi,T., Maki,H. and Akiyama,M. (2008) Overproduction of *Escherichia coli* DNA polymerase DinB (Pol IV) inhibits replication fork progression and is lethal. *Mol. Microbiol.*, **70**, 608–622.
67. Kim,S.R., Maenhaut-Michel,G., Yamada,M., Yamamoto,Y., Matsui,K., Sofuni,T., Nohmi,T. and Ohmori,H. (1997) Multiple pathways for SOS-induced mutagenesis in Escherichia coli: an overexpression of dinB/dinP results in strongly enhancing mutagenesis in the absence of any exogenous treatment to damage DNA. *Proc. Natl. Acad. Sci. U.S.A.*, **94**, 13792–13797.
68. Ho,H.N., Van Oijen,A.M. and Ghodke,H. (2018) The transcription-repair coupling factor mfd associates with RNA polymerase in the absence of exogenous damage. *Nat. Commun.*, **9**, 1570.
69. Heltzel,J.M.H., Scouten Ponticelli,S.K., Sanders,L.H., Duzen,J.M., Cody,V., Pace,J., Snell,E.H. and Sutton,M.D. (2009) Sliding clamp–DNA interactions are required for viability and contribute to DNA polymerase management in Escherichia coli. *J. Mol. Biol.*, **387**, 74–91.
70. Costes,A., Lecointe,F., McGovern,S., Quevillon-Cheruel,S. and Polard,P. (2010) The C-terminal domain of the bacterial SSB protein acts as a DNA maintenance hub at active chromosome replication forks. *PLoS Genet.*, **6**, e1001238.

Received: October 6, 2023. **Revised:** July 3, 2024. **Editorial Decision:** July 4, 2024. **Accepted:** July 8, 2024